공학박사 학위논문

Regulation of viability and differentiation of human stem cells *via* size-controlled graphene oxide flakes

크기가 조절된 산화 그래핀 플레이크를 이용한
인간줄기세포의 세포 활성 및 분화 조절

2023 년 2 월

서울대학교 대학원

공과대학 화학생물공학부

박 소 라

Chemical and Biological Engineering Major

Regulation of viability and differentiation of human stem cells *via* size-controlled graphene oxide flakes

지도교수 박 태 현

이 논문을 공학박사 학위논문으로 제출함

2023 년 2 월

서울대학교 대학원

공과대학 화학생물공학부

박 소 라

박소라의 박사 학위논문을 인준함

2023 년 2 월

위 원 장 김 병 수 (인)

부위원장 박 태 현 (인)

위 원 황 석 연 (인)

위 원 김 정 아 (인)

위 원 박 희 호 (인)

Abstract

Regulation of viability and differentiation of human stem cells *via* size-controlled graphene oxide flakes

Sora Park

School of Chemical and Biological Engineering

The Graduate School

Seoul National University

There is increasing interest in studying stem cell differentiation through cellular physical stimulation which can be translated into cell-recognized tension. It has been known that physical stimulation can direct human mesenchymal stem cell differentiation which called mechanotransduction. Recently, graphene oxide (GO), major derivative of graphene, has been synthesized as promising material which has suitable physico-chemical characteristics for stem cell lineage specification. GO can interact with integrin, the transmembrane receptor protein, through electrostatic, hydrophobic interactions. However, GO used in previous stem cell research has used GO with an irregular morphology and size. Such irregularity of GO causes diverse cellular responses according to lateral sizes of GO. In this study, we fabricated graphite mechanically with narrow size distribution by adjusting the ball-milling time. Then, size-controlled GO flakes were chemically

synthesized from ball-milled graphite using modified Hummer's method. Size distribution of GO were measured by hydrodynamic situations. Dose-dependent cytotoxicity of the size-controlled GO flakes on human stem cells was observed. The interaction between GO flakes and cells was analysed with electron microscopy. Also, effect of GO with osteogenic and neural differentiation of hMSCs were measured by staining and gene expression level. Also, by analyzing the shape and size of the cells through immunostaining, we confirmed that focal adhesion was key component involved in promoting stem cell differentiation and enhanced cell viability in apoptotic circumstances. We suggest that the size-controlled GO sheets would be efficient candidate for enhancement of lineage determination of human stem cells and therapeutic applications.

Keywords: Stem cell differentiation, Graphene oxide, Osteogenic differentiation, Neural differentiation, Apoptosis, Mechanotransduction

Student Number: 2016-21027

Contents

List of figures and table

List of abbreviations

ALP: alkaline phosphatase

bFGF: basic fibroblast growth factor

hMSC: bone marrow-derived human mesenchymal stem cell

ADSCs: adipose-derived human mesenchymal stem cell

BSA: bovine serum albumin

CCK-8: cell counting kit-8

cDNA: complementary deoxyribonucleic acid

CLSM: confocal laser scanning microscopy

DAPI: 4',6-diamidino-2-phenylindole

DMEM: Dulbecco's modified eagle medium

DMSO: dimethyl sulfoxide

E8: essential 8 medium

ECM: extracellular matrix

EthD-1: ethidium homodimer-1

FAK: focal adhesion kinase

FBS: fetal bovine serum

FF: feeder-free

GAP43: growth associated protein 43

GAPDH: glyceraldehyde 3-phosphate dehydrogenase

GDNF: glial cell line-derived neurotrophic growth factor

GFAP: glial fibrillary acidic protein

GO: graphene oxide

hEB: human embryoid body

hESCs: human embryonic stem cell

hMSC: human mesenchymal stem cell

HRP: horseradish peroxidase

ICC: immunocytochemistry

ICP-AES: inductively coupled plasma atomic emission spectroscopy

MAP2: microtubule-associated protein 2

MMC: mitomycin C

MNP: magnetic nanoparticle

mRNA: messenger ribonucleic acid

MSGM: magnetic spirillum growth medium

NdFeB: neodymium iron boron

NES: nestin

NPC: neural progenitor cell

OCT4: octamer-binding transcription factor 4

PAX6: paired box 6

PBS: phosphate buffered saline

PBST: triton X-100 in phosphate buffered saline

PCR: reverse transcription polymerase chain reaction

PFA: paraformaldehyde

PS: penicillin and streptomycin

ROCK: rho-associated protein kinase

RT-PCR: reverse transcription polymerase chain reaction

RUNX1: runt-related transcription factor 1

SDS-PAGE: sodium dodecyl sulfate polyacrylamide gel electrophoresis

SOX2: sex determining region Y-box 2

TE: trypsin-ethylenediaminetetraacetic acid

TEM: transmission electron microscopy

TUBB3: class III beta tubulin

Chapter 1

Research background and objectives

Chapter 1. Research background and objectives

Numerous recent reports conclude that stem cells pose boundless possibilities in the field of regenerative medicine for their multipotent ability to regenerate desired cells in the human body [1]. Among these stem cells, mesenchymal stem cells (MSCs), initially isolated from bone marrow, have been widely used for both research and commercialization purposes, owing to their accessibility, versatility, and low risk of teratoma formation [2]. The MSCs are also known to be capable of sprouting into various types of cells, including osteoblasts, chondrocytes, cardiomyocytes, and adipocytes, all of which play a quintessential role in the regeneration and reconstruction of most human body components. To guarantee the successful production of desired cells, as well as to maximize the regeneration efficiency, however, the characteristics of MSCs should be properly and precisely tuned prior to transplantation through the process termed 'differentiation', because their very ability to develop into multiple types of cells may also result in the production of unwanted cells [3].

The differentiation of stem cells is known to be governed by both insoluble cues (i.e. physical stimulus) and soluble cues (i.e. biochemical stimulus), or the combination of the two [4]. Biochemical stimulus, in the form of defined culture media, is predominantly utilized in guiding the differentiation of human MSCs (hMSCs) into the desired cell types. However, recent findings suggest that manipulating biophysical stimuli, such as the mechanical characteristics and topography of the substrates, could also play a critical role in directing the conversion of hMSCs into specific cell types of interest. Insoluble cues, commonly denoted as physical cues, encompass both topographical and mechanical properties that arise from the microenvironment of the cell [5]. The mechanical stimulus is normally induced through cell-substrate interactions, which consequently alter both the cytoskeletal dynamics and the gene expressions of the cells. Numerous studies have reported successful cases where the controlled introduction of various mechanical stimuli resulted in a desired manipulation of diverse cellular behavior in the course of the

differentiation of stem cells [6]. As an attempt to achieve favorable biophysical stimuli, nanostructure, microstructure, micropattern, and nanohybrid materials have recently been considered as novel approaches to guide stem cell differentiation, with or without using biochemical cues.

Graphene and its derivatives, such as graphene oxide (GO), have been regarded as attractive substrates for their unique capability to induce necessary physical stimuli for stem cell proliferation and differentiation[7]. For example, cell culture on GO-coated surfaces promoted cell adhesion and growth, and osteogenic differentiation of human MSCs (hMSCs) [8]. This is due to, as previously mentioned, the unique physicochemical properties of GO and the effects of the controlled geometry of GO patterns on stem cell compartments (e.g., integrin clustering, cytoskeletal reorganization, and activation of adhesion-related genes) [9].

In addition, ball-milling is an effective GO production method through the top-down approach of graphite, and it is possible to produce highly reproducible in a simple way through a standardized protocol [10]. There have been attempts to use these strategies in industrial applications, and this is the first time that it has been applied to stem cell research. Also, it has been reported that the distinct physicochemical characteristics of graphene and its derivatives cause the MSCs and neural stem cells (NSCs) to initiate several different types of differentiation, such as adipogenic differentiation, osteogenesis, oligodendrogenesis, and neurogenesis [11-13]. Some of these distinct physiochemical characteristics of interest pertain to multifarious surface chemistry, amphiphilicity, and unique carbon structure, all of which reportedly affects cell spreading, morphology, and the rate of absorption of proteins and chemicals in the defined culture medium. Specifically, Lee et al. [8] reported the different capabilities of graphene and GO to guide the osteogenesis of the MSCs, showing that their difference led to modified absorption of several osteogenic differentiation factors, e.g. dexamethasone, glycerophosphate, and ascorbic acid. In light of the profound influence of the chemical properties and geometries of nanomaterials, especially those of the graphene derivatives, on stem cell differentiation mentioned above, numerous studies have reported the application

strategies of graphene derivatives for efficient differentiation into specific lineages. In particular, graphene oxide micropatterns (e.g. square, line grid), graphene nanogrid, and graphene matrix were shown to efficiently enhance the differentiation of MSCs into osteoblasts, chondrocytes, and neurons [14]. This is attributed to the distinct physicochemical properties of GO as aforementioned, and the effects of the controlled geometry of GO patterns on stem cell compartments e.g. integrin clustering, cytoskeletal reconstruction, and activation of adhesion-related genes.

The increasing interest in the application of GO derivatives to stem cell differentiation has provided momentous opportunities for stem cell lineage control. However, the effects of graphene lateral size on the behaviors of stem cells – some of the most critical factors – have not been fully understood, which might prevent the full potential of GO-based materials for stem cell research from being realized, especially for guiding stem cell differentiation into specific lineages based on GO-induced physicochemical stimuli. In view of the fact that the GO sheet size is important in determining the cytotoxicity toward different types of cell lines, it follows that the difference in GO size could also play a critical role in stem cell behaviors, especially the ability to guide the differentiation of hMSCs [15].

Therefore, the size effects of GO on the differentiation of human stem cells, especially hMSCs specifically studied using size-controlled GO flakes. Through these studies, it will be possible to understand the behavior of human stem cells due to the differences in the physicochemical properties of graphene oxide and to effectively apply them to research on the development of stem cell therapeutics.

Chapter 2

Literature review

Chapter 2. Literature review

2.1. Human stem cells

2.1.1. Human mesenchymal stem cells

hMSC are fusiform, fibroblast-like cells. The cells are negative for hematopoietic surface markers: CD34, CD45, CD14 and positive for a variety of markers: Stro-1, CD29, CD 73, CD90, CD105, CD166 and CD44 [16]. Differences exist among the reported studies in the surface marker characteristics that may be explained by variations in culture methods and/or differentiation stage of the cells. However, a number of surface markers has been suggested by a working group within the International Society for Cytotherapy as a minimum criterion for defining the cells as MSC.1 Traditionally, hMSC have been isolated from low-density mononuclear cell population of bone marrow, based on their selective adherence, compared to hematopoietic cells, to plastic surfaces [17]. One disadvantage of this method is the unavoidable hematopoietic cell contamination and the cellular heterogeneity of cultures with respect of differentiation potential. The concept of cellular 'heterogeneity' of MSC refers to differences in the differentiation potential among single-cell clones of MSC. For example, in vitro single-cell cloning of hMSC has demonstrated that only around 30% of the clonal MSC (that is, CFU-f) are multipotential and thus true MSC.14 However, there are no current surface markers that can be employed to isolate the multipotent MSC prospectively.

2.1.2. Human embryonic stem cells

hESCs are derived from preimplantation stage embryos, a process that involves culturing embryos to the morula or blastocyst stage (see below). In most cases, these embryos are donated for research after being targeted for discard either because they are excess embryos or because they are of poor quality. Initial derivations of hESCs performed in the Thomson laboratory at the University of Wisconsin (Madison, WI, USA) were isolated from the ICM of human blastocysts and placed on

inactivated murine feeder cells (MEFs) [18]. The resulting cell population was then maintained as a cell line by continuous subculture. Several labs have since published the derivation of additional lines using similar protocols including derivation on lysed MEFs or human feeders [19].

Developing improved technology for the genetic manipulation of hESCs will also be crucial for their effective application in research. Although hESCs can be modified by transgenesis and gene targeting, there are still questions about the efficiency of the techniques in different cell lines. The generation of stable transformants of hESCs has been achieved using conventional DNA delivery systems, or through the use of lentiviral or adenoviral vectors [20]. One group used gene targeting via electroporation to obtain homologous recombination in hESCs at frequencies similar to those observed in mouse ES cells. The use of short interfering (si)RNA to knockdown gene expression is another methodology that holds promise for use in ES cell research, and several recent reports have shown that this technique can be used to knockdown gene expression in ES cells [21].

2.2. Stem cell research utilizing graphene oxide

Graphene is a form of carbon atoms in a two-dimensional honeycomb structure. It has been intensively studied and is known to possess several unique properties such as high opacity (~97.7%), excellent electrical conduction ability (carrier mobility: 10000 cm2·V−1·s−1), and superior mechanical strength (Young's modulus: 1100 GPa), which have propelled the utilization of graphene for electronic, electrochemical, and optical applications [12]. Besides the aforementioned characteristics, recent studies have also uncovered a number of fascinating properties of graphene, including high photoconversion efficiency, tunable amphiphilicity, excellent drug loading capacity, flexibility in size, and low cytotoxicity, all of which are useful features for nanomaterial-based biomedical applications such as cancer and stem cell therapies [22].

Compared to their use in cancer research, the use of graphene-based materials in stem cell applications is a relatively new area of research. As discussed in numerous research articles, stem cells have emerged as one of the most promising candidates for regenerative therapies because of

their unique properties of self-renewal and differentiation. It is predicted that differentiated stem cells will be implantable in various tissues, which will ultimately be useful for the treatment of a wide range of diseases. Although promising, there are several issues that hinder the practicality of stem cells for regenerative therapies, including (1) low ex vivo differentiation efficiency; (2) low engraftment efficiency after transplantation; and (3) lack of the tools that would allow scientists and doctors to rapidly, easily, and precisely implant stem cells without sacrificing their viability and functionality [23].

The most common method for guiding the differentiation of stem cells involves the use of soluble factors including proteins, small molecules, and mixed supplements, all of which have to be carefully tuned based on the individual application [24]. In addition to the soluble cues, it has been reported that insoluble cues, which encompass the establishment and manipulation of extracellular microenvironments, especially the underlying substrates wherein cells attach and grow, have significant roles in controlling stem cell behaviors such as migration, proliferation, differentiation, and apoptosis. Interestingly, graphene has proven to be capable of directing stem cell differentiation into specific cell types such as neurons, oligodendrocytes, osteoblasts, and adipocytes, based on the type of material (e.g., graphene, graphene oxide, and graphene hybrid scaffolds), as well as the type of progenitor cell (e.g., neural stem cells and mesenchymal stem cells) [25]. It can be used to tune such physical properties as elasticity, porosity, and micro/nanostructure.

Besides the ability of graphene derivatives to guide the differentiation of stem cells, graphene has shown immense potential as an implantable material; it can help stabilize the growth and differentiation of stem cells embedded in three-dimensional hydrogels, thereby enhancing the efficiency of engraftment after transplantation [26]. Additionally, graphene has value as a detection molecule. Its surface absorbs specific molecules released from cells or embedded on cell membranes and enhances optical and/or electrical signals detectable by external analytical techniques. Hence, despite a short history of utilization, considering the impact of stem cell-based regenerative therapies,

it is worthwhile to summarize and highlight the recent progress of the use of graphene and/or graphene-based hybrid scaffolds for stem cell applications.

Therefore, in this review, we will discuss the biomedical applications of graphene-based materials, with a particular focus on guiding stem cell differentiation, stem cell transplantation/delivery, and monitoring/detection of stem cell differentiation. There are several review articles that discuss the use of graphene derivatives as therapeutic materials [27]. However, the utilization of graphene-based materials for stem cell applications is a rapidly emerging area and, thus, needs to be highlighted in order to fully understand their applicability and to envision the full potential of graphene in stem cell research.

Chapter 3

Experimental procedures

Chapter 3. Experimental procedures

3.1. Preparation of GO

3.1.1. Ball-milling of graphite

Pristine graphite powder (5.5 g) was placed into a planetary grinding zirconia bowl with zirconia grinding balls (1, 2, and 5 mm in diameter) [28]. The bowl was fastened in a planetary mono mill (PULVERISETTE 6, FRITSCH) and rotated at 550 rpm for different durations (30, 60, and 90 min). Ball-milled graphite powders were collected using U.S.A. standard sieves.

3.1.2. Preparation of GO by ball-milled graphite

Graphite (flakes, < 20 μm) was purchased from Sigma-Aldrich. Graphene oxide was synthesized with the improved Hummers' method [29]. Sodium nitrate (0.5 g) was dissolved in the mixture of concentrated sulfuric acid and phosphoric acid. The collected ball-milled graphite powder was dispersed homogeneously. Potassium permanganate was placed slowly in an ice bath and maintained at 50°C overnight. Afterward, the solution was poured into 200 mL of ice. Finally, hydrogen peroxide solution (1 wt%) was added to finish the oxidation. After mild sonication for 1 h, the sample was washed repeatedly with 5% hydrochloric solution (Sigma) and deionized water. It was then dried in a vacuum oven at 50°C for 24 h.

3.2. Characterization of GO

TEM images were acquired using a JEM-2100 microscope (JEOL Ltd., Japan) installed at the National Center for Inter-university Research Facilities (NCIRF) at Seoul National University. Size distribution of GO was assessed with a zeta potential and mean particle diameter analyzer (ELSZ-1000, Otsuka Electronics). A Raman spectrometer (T64000, Horiba Scientific) was used to analyze vibrational modes of GO. The excitation wavelength of the laser was 532 nm. All samples were pelletized at a pressure of 7 metric tons for standardization of Raman resolution. X-ray photoelectron

spectroscopy (XPS) spectra were measured using a Sigma probe (ThermoVG). FT-IR spectra were collected with a Frontier spectrophotometer (PerkinElmer).

3.3. Preparation of magnetic nanoparticles

Magnetic nanoparticles (MNPs, Fe_3O_4), obtained from an anaerobic magnetotactic bacterium (*Magnetospirillum* sp. AMB-1, ATCC), were used to generate 3D human embryonic stem cells (hESCs), called human embryoid bodies (hEBs). The magnetic bacterium was cultured in a modified magnetic spirillum growth medium (MSGM), as previously described [30, 31]. In brief, bacteria were cultivated *via* a fermenter (FMT-ST-S05, Fermentec) in an anaerobic condition for 5 days at 27 °C. Then the bacterial cells were centrifuged at 11,300 × g for 20 min, and then the collected cells were sonicated with 35% amplification for 15 min (VCX500, Sonics & Materials). The MNPs were isolated from bacterial cell debris using 100 mm Petri dishes with neodymium-iron-boron (NdFeB) magnets attached below. Only MNPs, except for cell debris, were attached along the perimeter of the magnets. Therefore, the MNPs were collected while the cell debris was washed out. The separated MNPs were washed 3 times using phosphate-buffered saline (PBS; Welgene), relying on magnetic adhesion. Then the MNPs were sterilized using an autoclave. After measuring the concentration of iron ions using ICP-AES (ICPS-7500, Shimadzu), the MNPs were stored in a concentration of 1 mg/ml in PBS at 4 °C. Before use, the MNPs were dispersed using bath type ultrasonicator (JAC 1002, Kodo Technical Research) for 10 min.

3.4. Cultivation and differentiation of hMSCs

Human mesenchymal stem cells (hMSCs, Lonza) were purchased at passage 2 and used at passages 3-5. hMSCs were maintained in T-75 tissue culture flasks (SPL) until 80% confluency and then detached and transferred using 0.25% trypsin-EDTA (Gibco). The maintenance medium was MEM Alpha GlutaMAX^{TM} (Gibco) supplemented with 10% fetal bovine serum (FBS; Biowest), 1% Penicillin-Streptomycin (PS; Gibco), 100 μg/ml Primocin (Invitrogen). To induce osteogenic

differentiation of hMSCs, MEM Alpha GlutaMAX™ supplemented with 10% FBS, 1% PS, 10 mM β-glycerophosphate disodium salt hydrate (Sigma), 100 μg/ml Primocin, 50 μg/ml ascorbic-2-phosphate (Sigma), and 100 nM dexamethasone (Sigma) was used with 10 μg/ml graphene oxide in corresponding experimental groups [32, 33]. The medium was replaced with a fresh medium every two days.

3.5. Cultivation of hESCs

hESCs (SNUhES31) were supplied in passage 23 from the Seoul National University Medical Research Center upon approval from the Seoul National University Institutional Review Board (IRB No.1402/002-006). hESCs were maintained in standard hESC growth condition and sustained their pluripotency, following previously described protocols [19, 34]. Briefly, the hESCs were cultured with STO mouse fibroblast cells (STO cells), which were mitotically inactivated by mitomycin C (MMC; Sigma), on 0.2% gelatin-coated cell culture dishes in Dulbecco's Modified Eagle Medium with Nutrient Mixture F-12 (DMEM / F-12, Gibco) supplemented with 20% KnockOut™ Serum Replacement (Gibco), 4 ng/ml basic fibroblast growth factor (Invitrogen), 0.1 mM β-mercaptoethanol (Sigma), 0.1 mM nonessential amino acids (Gibco) and 50 units/ml penicillin and 50 μg/ml streptomycin (Gibco). For subculture, the hESC colonies were disassembled by modified Pasteur pipettes and re-plated on new dishes with a fresh STO feeder layer, every 5 to 7 days. The medium of hESCs was daily replaced. The passages of hESCs utilized in this study were between 32 to 42.

For feeder-free culture, hESCs were transferred to dishes coated with Geltrex™ (Gibco), and their culture medium was switched to Essential 8™ medium (Gibco) without any influences on pluripotency [15]. Cells were cultivated at 37 °C with 5% CO_2 in a humidified incubator.

3.6. Generation of hEBs and neural differentiation

First, 96-well non-coated round bottom plate (SPL) was coated with 0.1% F-Pluronic 127 (Sigma) in double distilled water for 1 h. Feeder-free hESCs were detached with accutase (Millipore) and 1 × 10^4 cells were added to the well in order to generate hEBs without MNPs (hEBs + NIM + MNPs).

Second, the feeder-free hESCs were treated with 20 μg/ml of MNPs for 24 hrs. The MNP-incorporated hESCs were detached with accutase and then sufficiently magnetized hESCs were isolated by the NdFeB magnets for 1 min. After separation of MNP-hESCs, the suspended cells were applied to concentrated magnetic pin system, which was manufactured as described in the previous work [35]. In brief, the lids of 96-well plates were prepared with NdFeB magnets (10 mm × 5 mm × 6 mm) placed upon the lids, and iron pins attached to the magnets under the lids. 1 × 10^4 cells in a volume of 130 to 135 μl were added to each well. Then the magnetized hESCs were gathered toward the iron pin at which magnetic force was concentrated, resulting in generation of MNP-hEBs underneath the medium surface (hEBs+ NIM + MNPs).

For initial neural differentiation, 2D and 3D hESCs were cultured in neural induction medium (NIM; Gibco, 21103049) for 5 days. The medium was changed on the 3rd day. Cells were cultured at 37 ℃ with 5% CO_2 in a humidified incubator.

3.7. Cell adhesion assay of GO

hMSCs were observed by transmission electron microscopy (TEM) and field emission scanning electron microscopy (FE-SEM) to obtain images of GO flakes bound to the cell membrane of hMSCs [36]. hMSCs were fixed with paraformaldehyde-glutaraldehyde solution (Karnovsky's Fixative) for 2 h at 4℃. These cells were then washed with 0.05 M sodium cacodylate buffer. Subsequently, cells were fixed with 2% osmium tetroxide in 0.1 M cacodylate buffer for 2 h and washed with distilled water, followed by overnight incubation with 0.5% uranyl acetate for negative staining at 4℃. After serial dehydration with sequentially concentrated ethanol from 30% to 100%, TEM samples were treated with propylene oxide to remove residual ethanol. Finally, TEM samples

were transferred to a resin polymer with propylene oxide to be embedded. These resin samples were cut using an ultramicrotome (EM UC7, Leica, Germany) and then observed using a TEM (JEM1010, JEOL, Japan). SEM samples were investigated in a mount and observed with an FE-SEM (JSM1010, JEOL, Japan).

3.8. Cell viability assay

3.8.1. CCK8 assay

To examine the cytotoxicity of GO to hMSCs, a Cell Counting Kit-8 (CCK-8, Dojindo, USA) was used [37]. In brief, after incubating hMSCs with GO for 24 h in a humidified CO_2 incubator at 37°C, CCK-8 solution was added to cells at 10% concentration. After incubating in the humidified CO_2 incubator at 37°C for another 2 h, the absorbance of each well was measured at a wavelength of 450 nm with a microplate reader (Tecan, Switzerland).

3.8.2 Fluorescence-based live and dead assay

In order to detect the live and dead cells, LIVE/DEAD cell viability kit (Molecular Probes, USA) was used. The cells were treated with a mixed solution of 2 μM acetoxymethyl ester of calcein (calcein AM) and 4 μM ethidium homodimer-1 (EthD-1). After incubation for 1 h at 37 °C in a humidified CO_2 incubator, green fluorescence for live cells and red fluorescence for dead cells were observed.

3.9. qRT-PCR analysis

To analyze the osteogenic differentiation of hMSCs, relative expression levels of osteogenic genes was measured. Total RNA was extracted using TRIzol® RNA Isolation Reagents (Invitrogen) according to the manufacturer's instructions. Then 500 ng of total RNA of each sample was used for cDNA synthesis with an M-MLV cDNA synthesis kit (Enzynomics, South Korea) following the manufacturer's instruction. Quantitative real-time reverse transcription-polymerase chain reaction (qRT-PCR) was performed with a StepOnePlus™ Real-Time PCR System (Applied Biosystems,

USA) using TOPreal™ qPCR 2X PreMIX (Enzynomics, South Korea). Expression levels of genes were normalized against the expression level of glyceraldehyde 3-phosphate dehydrogenase (*GAPDH*), a housekeeping gene. To determine early osteogenic differentiation, primers specific for runt-related transcription factor 2 (*RUNX2*) were used. Primers specific for osteopontin (*SPP1*) and integrin-binding sialoprotein (*IBSP*) were used as middle and latter osteogenic differentiation markers, respectively. Focal adhesion kinase (*PTK2*), paxillin (*PXN*), talin (*TLN*), and yes-associated protein (*YAP*) gene were analyzed to assess expression levels of focal adhesion complex and mechanosensing. Sequences of primers used in this study are listed in Table. 1.

Gene			Primer sequence (5'→3')	T_m (℃)	Product size (bp)
Housekeeping gene	*GAPDH*	F	TTCACCACCATGGAGAAGGC	59.96	256
		R	TCTTCTGGGTGGCAGTGATG	59.67	
Osteogenic marker gene	*RUNX2*	F	GCGCATTCCTCATCCCAGTA	59.89	176
		R	GGCTCAGGTAGGAGGGGTAA	60.03	
	SPP1	F	GCCGAGGTGATAGTGTGGTT	59.75	261
		R	ATCTGGACTGCTTGTGGCTG	60.32	
	IBSP	F	ATCCAGCTTCCCAAGAAGGC	60.03	269
		R	CTTCCGGTCTCTGTGGTGTC	60.04	
Focal adhesion-related gene	*PTK2*	F	GCTCCCTTGCATCTTCCA	58.8	132
		R	TTGGGGTCAAGGTAAGCAGC	59.0	
	PXN	F	GGAAAAGTTGCGGGGCATAG	58.0	154
		R	CAAGAACACAGGCCGTTTGG	58.3	
	TLN	F	CGTGCAAACCAGGCAATTCA	57.7	150
		R	ATTGGTGGTACGGGCAGAAG	58.7	

Table 1. List of primers used in qRT-PCR

3.10. Alkaline phosphatase staining and Alizarin Red S staining

Alkaline phosphatase (ALP) activity was analyzed using a staining kit (Sigma), following the manufacturer's instructions [38]. For Alizarin Red S (ARS; Sigma) staining, cells were fixed with 4% paraformaldehyde (PFA) and stained with 2% ARS solution. Cells were washed with deionized water after each step. To quantify the number of deposited minerals, 10% cetylpyridinium chloride (Sigma) solution was used to dissolve the ARS stain for 30 min. The absorbance was measured at a wavelength of 545 nm with a microplate reader (Tecan).

3.11. Immunocytochemistry

hMSCs were put into confocal dishESC and fixed with 4% PFA for 10 min at room temperature (RT). After permeabilization using 0.25% Triton-X (Sigma) in 0.1% phosphate-buffered saline with Tween 20 (PBST) for 10 min at RT, hMSCs were blocked by 3% bovine serum albumin (BSA) in 0.1% PBST for 1 h at RT on a rocker. Primary antibodies targeting differentiation maker proteins were diluted with 1% BSA in 0.1% PBST according to the manufacturer's instruction. hMSCs were then incubated with primary antibodies at RT overnight on a rocker. For detecting osteogenic differentiation markers and focal adhesion, anti-type Wecollagen antibody (Abcam, ab34710), anti-osteopontin (OPN) antibody (Abcam, ab8448), Alexa flour 488-conjugated phalloidin (Invitrogen, A12379), and anti-FAK antibody (Abcam, ab81298) diluted at 1:1000 in 0.1% PBST were used. Alexa flour 594-conjugated phalloidin (Invitrogen, A12381), anti-RUNX2 antibody (Santacruz, sc-390351), and anti-YAP antibody (Santacruz, sc-101199) were also used to detect osteogenesis and YAP nuclear localization. Corresponding secondary antibodies (Alexa Flour 594®, Invitrogen) were then used.

3.12. Western blotting

After 3×10^5 cells were re-suspended in RIPA Buffer (LPS Solution) with protease inhibitor cocktail (Abcam, 1:100 dilution), cells were lysed for 15 min at RT. Cell lysates were then mixed

with 5X sulfate-polyacrylamide gel electrophoresis (SDS-PAGE) protein loading buffer (iNtRON) and boiled in a boiling water bath for 5 min. After 20 μl of each sample was loaded into each well of SDS-PAGE gel, proteins were separated by electrophoresis and transferred to nitrocellulose blotting membranes (GE Healthcare Life science). These membranes were blocked with 5% BSA in 0.1% PBST for 1 h at room temperature and then incubated with primary antibody in 1% BSA prepared with 0.1% PBST overnight at 4 ºC. After incubation with horseradish peroxidase (HRP)-conjugated secondary antibody in 5% BSA in 0.1% TBST (tris-buffered saline with Tween 20; 1:2000 dilution) for 1 h, membranes were treated with IgG-horseradish peroxidase (HRP; AbFrontier) and signals were measured with a G: BOX Chemi XL system (Syngene). Primary antibodies used for Western blotting included anti-RUNX2 antibody (Abcam), anti-p-FAK antibody (CUSABIO, CSB-RA018994A397phHU), anti-FAK antibody (Abcam), anti-p-MEK1/2 antibody (CUSABIO, CSBPA000569), anti-MEK1/2 antibody (CUSABIO, CSBPA013409LA01HU, CSB-PA04909A0Rb), anti-p-ERK1/2 antibody (Santacruz, sc7383), and anti-ERK1/2 antibody (Santacruz, sc-94). As a reference, β-actin antibody (Abcam, ab8227) was used.

3.13. Statistical analysis

The statistical analysis was conducted by repeatedly drawing results from samples of all groups. Statistical significance was determined by analysis of variance (*t*-test, SigmaPlot) and marked with asterisk (* for $p < 0.05$, ** for $p < 0.01$, and *** for $p < 0.001$).

Chapter 4

Material characteristics and cellular interactions of size-controlled graphene oxide flakes

Chapter 4. Material characteristics and cellular interactions of size-controlled graphene oxide flakes

4.1. Introduction

The quantitative determination of the lattice disorder present in graphene layers will be crucial if this 2-D material is to be commercialized. Raman spectroscopy has been shown to be a powerful technique for characterizing the density of these defects in graphene layers. Here, we study the evolution of Raman spectra with defect size, for vacancy defects created via ion bombardment. Raman spectroscopy was used to analyze the variation in the D-peak and G-peak intensity ratio for single-layer graphene, whilst the equivalent defects in highly ordered pyrolytic graphite were characterized using scanning tunneling microscopy to determine their lateral dimensions. Vacancy defects of larger lateral sizes were shown to have an associated coalescence of defects at a larger inter-defect distance, through changes in the intensity ratio of the D- and G-peaks, as well as the D-peak width. This is in agreement with a phenomenological model previously determined for calculating the defect density in graphene layers, and experimentally reveals the effect of graphene defect size for Raman spectroscopy measurements. Importantly, these results show how the graphene defect size must be obtained separately to allow the quantification of the graphene defect density using Raman spectroscopy.

4.2. Characterization of GO processed by ball-milling

To investigate effects of various sizes of GO on hMSCs, three groups of GOs with different size distributions were produced with varying ball-milling time durations of 30, 60, and 90 minutes. A total of four GO experimental groups including a group without ball-milling (GO-4.6) was prepared. Each experimental group was prepared with varying ball-milling time and named as GO-0.9, GO-1.1, GO-1.7, and GO-4.6 according to the average size of GO flakes in each group (Fig. 4.1). Fig.

4.1B shows changes in average lateral size of the prepared ball-milled graphene oxide flakes depending on ball-milling duration (30, 60, and 90 minutes). TEM images for GO-0.9, GO-1.1, GO-1.7, and GO-4.6 are shown from left to right. The GO produced through ball-milling showed a tendency to increase in size from about 900 nm to 5 μm with decreasing ball-milling time. Sizes of the three ball-milled GO groups with comparably regular round-shape were significantly reduced compared to those of the no ball-milling group (GO-4.6) which showed an irregular shape. The average value of the GO diameter of each GO group was analyzed by dynamic light scattering (DLS) for precise identification than using AFM. The size distribution of the ball-milled GO group was generally narrower than that of the GO-4.6 group (Fig. 4.1C).

AFM is one of the measurement tools for determining the diameter of nanomaterials through sample preparations such as the Langmuir-Blodgett method [39]. Notwithstanding, analyzing the size distribution by DLS when measuring the GO flakes has two advantages for this study. First, the hydrodynamic size of GO flakes can be measured in suspension state without additional sample preparation process. Second, we can guarantee a larger amount of the sample by DLS compared to AFM, since DLS identifies all the flakes in the suspension, whereas AFM can identify only those collected through pretreatment.

Although AFM can provide a rather accurate description of both lateral and vertical dimensions of a single flake as well as ensemble size distributions, the method is tedious and time-consuming as a large number of images must be recorded and analyzed, which rarely is the case. DLS, in comparison, facilitates a much faster and less expensive assessment of the average flake size and size distribution, although only equivalent size, the equivalent sphere hydrodynamic diameter, is determined. Since both methods have their limitations, DLS appears to be more advantageous compared with AFM for fast GO flake size assessment, especially when a large number of samples are to be analyzed and a relative size description, as opposed to an absolute size description, is sufficient. Also, other previous studies were also conducted in the same manner, we decided to utilize DLS in this study [40].

Fig. 4.1D shows deconvolution of C1s core level of XPS analysis to determine chemical species consisting of GO flakes. Spectra of GO flakes showed four characteristic peaks with binding energies of 284.5, 286.4, 287.2, and 287.7 eV attributed to C–C/C=C, C–OH, C–O–C, and C=O bonds, respectively. The intensity of the C–C/C=C peak originated from sp2-hybridized carbons [41]. Intensities of C–OH, C–O–C, and C=O species were greater in the three ball-milled GO groups than in the GO-4.6 group. For this reason, the degree of oxidation for the ball-milled GO group was larger than that of the non-ball-milled GO-4.6 group according to C1s and O1s spectra results (Fig. 4.2D, 4.2E). From these data, it can be inferred that as the average size of GO increases, the edge portion is less attacked by the oxidizing agent. Therefore, the distribution of functional groups such as C=O and O-H decreases and the oxidation degree decreases [42]. The chemical exfoliation process introduced oxygen functional groups into basal and edge planes of graphene. Active sites on the ball-milled GO surface could bind more oxygen functional groups because of the greatly increased surface area. Ball-milling reduced the particle size and concurrently increased the number of polar groups. Despite these vulnerabilities, the relatively large size of GO-1.7 was not significantly less oxidized than the relatively small GO-0.9 and GO-1.1 groups, unlike the least oxidized group, GO-4.6 (Fig. 4.1E). Thus, the effect of each GO group on hMSCs is relatively dependent on the size factor rather than the degree of oxidation.

Raman spectroscopy was utilized to discern changes in molecular morphology of the prepared GO flakes. All GO samples exhibited the G band at 1590 cm^{-1} and the D band at 1350 cm^{-1} as the two main characteristic bands of graphitic materials (Fig. 4.2A). The G band represents in-plane sp2 C–C stretching mode, while the D band is known as a double resonant process induced by scattering from a defect [43]. Ball-milling pretreatment of graphite powders promoted both a decrease in in-plane graphitic domain size and an increment in the number of various defects. As a result, as shown in Fig. S1B, the value of the I_D/I_G intensity ratio is a measurement of disorder degree. When the graphite precursor was ball-milled for 90 min (GO-0.9), 60 min (GO-1.1), or 30 min (GO-1.7), the I_D/I_G ratio was 1.074, 1.036, or 1.027 for ball-milled graphene oxide, respectively, indicating that

ball-milling tore the graphitic structure in sunder (Fig. 4.1B). As I_D/I_G value decreases, the degree of oxidation decreases. Of the three ball-milled GO groups, it was assumed that GO-0.9 and GO-1.7 had more oxidative functional groups than the GO-1.1 group. A previous study has reported that ball-milling can reduce GO particles to submicrometer sizes and concurrently transform the particle morphology from flake to spherical, with a slight decrease in density [10].

Attenuated total reflection (ATR) Fourier-transform infrared (FTIR) spectra were investigated to identify chemical bonds of GO flakes (Fig. 4.2C). In general, the overall intensity of characteristic peaks is weakened with a longer milling time. Furthermore, C–H stretching vibrations at 3130 and 3050 cm-1 became more intense in GO-1.7 than in GO-0.9 and GO-1.1 groups. The strong band around 3400 cm^{-1} attributed to O–H stretching vibrations increased in intensity with increasing milling duration. The C=O stretching vibration at 1730 cm^{-1} was also increased. On the other hand, the C=C stretching vibrations at 1620 cm^{-1} diminished, implying that graphitic rings were damaged in the oxidation process and changed into oxygen-containing functional groups [44]. Overall, oxidative functional groups were recruited more in ball-milled GO groups than in the non-ball-milled GO-4.6 group.

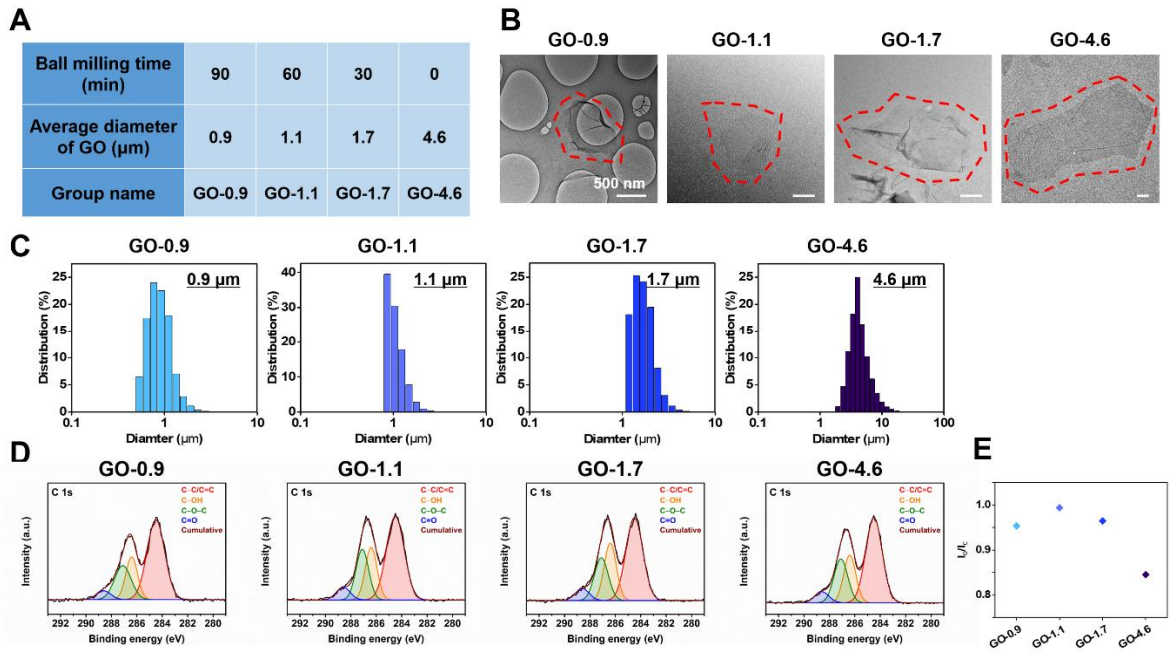

Figure 4.1. Synthesis and characterization of physical properties of GO. (A) Assigned names of experimental groups by their average hydrodynamic diameter. The more the ball-milling time, the smaller the GO flakes. (B) Morphology and wrinkled structure of GO were analyzed by TEM. (C) The size distribution of each group of GO was analyzed by DLS. (D) Deconvolution of XPS spectra for GO flakes (from left to right: GO-0.9, GO-1.1, GO-1.7, and GO-4.6). (E) XPS intensity ratio of oxygen and carbon peaks. GO-4.6 had relatively low oxygen-containing groups than other groups.

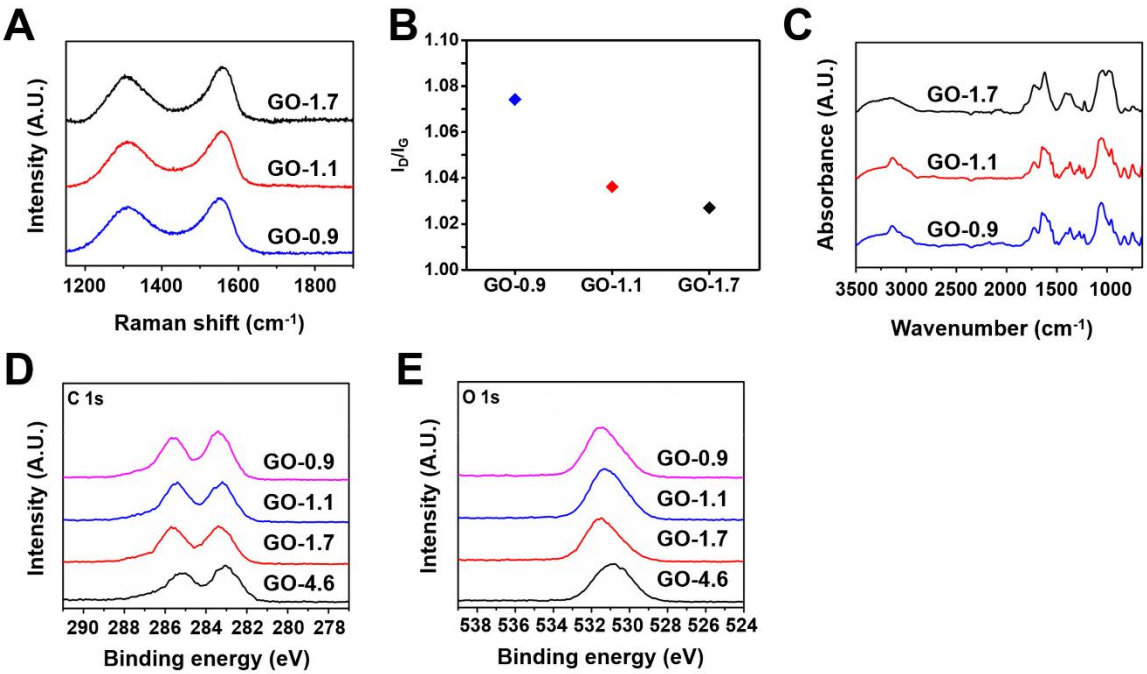

Figure 4.2. Detailed characterization of graphene oxide (GO). (A-B) Raman spectra of GO and the calculated value of [D peak area versus G peak area] in Raman spectra. The longer the ball-milling time, the higher the value of [D peak area versus G peak area]. (C) FT-IR spectra of GO. Conventional peaks observed in GO were found and several peaks were assigned due to damage to the intact graphene structure. (D-E) C1s XPS spectra of GO and O1s XPS spectra of GO showing distribution of surface functional groups on each GO group.

4.3. Morphology and cytotoxic effect of GO attached to hMSCs

Fig. 4.3A shows representative SEM images, which is the morphology of GO flakes on the surface of hMSCs. GO in the form of a flake was attached to the outside of the cell membrane. After affixing cells to a cover slide glass and magnifying the edge of the cell membrane, the GO in the form of a flake was detected to be attached to the outside of the cell membrane. While the surface of the control cells was smooth, the surface of GO-treated cells showed a rough and wrinkled structure due to the attached graphene oxide [45]. TEM images in Fig. 4.3B show cell edge treated with GO (black arrows). The cell was cut in the form of a pellet and GO was shown as a solid line. However, in SEM, GO flakes was shown in the form of a plane. GO appearing like a solid line on the cell surface was observed only on the surface, not inside the cell. Several studies have reported that nano-sized GO is internalized into cells, whereas GO used in this experiment was confirmed to attach only to the edge of the cell [46].

The cytotoxicity of GO to hMSCs was evaluated by measuring the viability of hMSCs after 24 hours of treatment (Fig. 4.3C). A previous research has reported that GO might be cytotoxic in a dose-dependent manner [47]. Cytotoxicity of GO generally showed a tendency to increase with increasing concentration of GO in all groups. The experiment was conducted at a concentration of 10 μg/ml, which showed a relatively low toxicity (over 8-90% of viability). In addition, proliferation during 21 days of osteogenic differentiation was investigated to assess the long-term cytotoxicity of GO. Data of each group were then compared with the control on day 7 (Fig. 4.3D). After 21 days of differentiation, the viability of hMSCs was decreased in all groups treated with GO compared to that of the control group, which showed a relatively long-term toxicity of graphene oxide materials. In particular, the GO-4.6 group showed a noticeable cytotoxicity, consistent with previous results reported size-dependent toxicity of graphene materials [48]. The modification by oxidative functionalization of graphene surfaces revealed differential hydrophilicity; their hydrophilicity increased with the increased oxygen content, consistent with the findings of Chatterjee et al. Aggregation of graphene due to low dispersion in exposure medium is attributed as one the major

reasons for the difference in degree and mode of cytotoxicity [49]. Pristine graphene, which readily aggregates, due to its hydrophobic nature (extensive sp2 carbon backbone), and largely in the exposure medium it induced a significant reduction in cell viability even at 5 μg ml−1 concentration as compared to the control. These results support the hypothesis that pristine graphene cytotoxicity, even at the lower exposure doses, could possibly occur due to the hydrophobic sheets or aggregates interacting with and absorbing vital nutrients or cell signaling molecules necessary for cell survival [50]. As a result, in the three ball-milled GO groups except for the GO-4.6 group, although the cytotoxicity was significant compared to the control group, cells proliferated over 21 days of osteogenic differentiation.

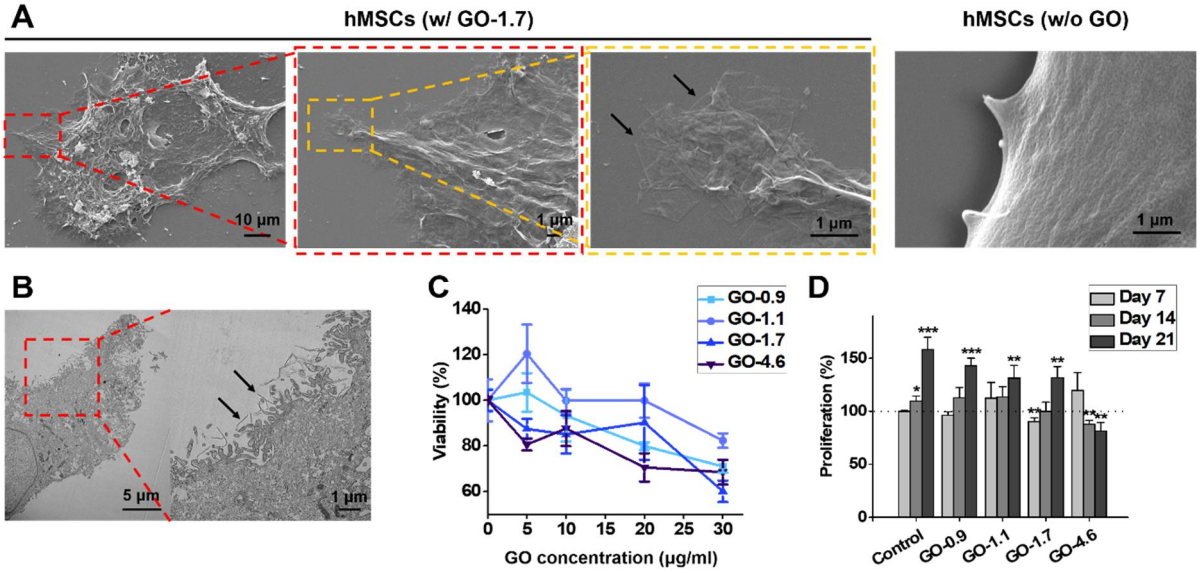

Figure 4.3. **Morphology of GO on the surface of hMSCs and cytotoxicity of GO.** (A) Planar morphologies of GO on the surface of hMSCs and hMSCs without GO were analyzed by SEM. The surface of hMSCs with GO-1.7 showed ruffling and shedding whereas the surface of hMSCs without GO was smooth. (B) Vertical morphology of GO on the surface of hMSCs was analyzed by TEM. Black arrows indicate vertical morphology of GO flakes. (C) Dose-dependent cytotoxicity of GO to hMSCs after 24 hours of treatment (n = 5). The concentration of 10 μg/ml was selected for the application, which showed a relatively high viability of 80 to 90% in all groups. (D) Proliferation of hMSCs during osteogenic differentiation for 21 days. All values were normalized and compared statistically with the value of the control group on day 7 (n = 5).

4.4. Conclusions

To investigate effects of various sizes of GO on hMSCs, three groups of GOs with different size distributions were produced with varying ball-milling time durations of 30, 60, and 90 minutes. The effect of each GO group on hMSCs is relatively dependent on the size factor rather than the degree of oxidation. Overall, oxidative functional groups were recruited more in ball-milled GO groups than in the non-ball-milled GO-4.6 group. After 21 days of differentiation, the viability of hMSCs was decreased in all groups treated with GO compared to that of the control group, which showed a relatively long-term toxicity of graphene oxide materials. In particular, the GO-4.6 group showed a noticeable cytotoxicity, consistent with previous results reported size-dependent toxicity of graphene materials. As a result, in the three ball-milled GO groups except for the GO-4.6 group, although the cytotoxicity was significant compared to the control group, cells proliferated over 21 days of osteogenic differentiation.

Chapter 5

Enhanced osteogenic differentiation of bone marrow-derived human mesenchymal stem cells using size-controlled graphene oxide flakes

Chapter 5. Enhanced osteogenic differentiation of bone marrow-derived human mesenchymal stem cells using size-controlled graphene oxide flakes

5.1. Introduction

Among various applications of graphene, this paper focused on the lateral size of graphene oxide (GO) flakes and responses of bone marrow-derived human mesenchymal stem cells (BM-hMSCs). It has been reported that the cytotoxicity of a graphene material depends on its lateral size whereas the effect to stem cell lineage determination was less studied [48-52]. In a recent study, when micro graphene oxide (MGO) and nano graphene oxide (NGO) were applied to osteogenic differentiation of human adipose-derived mesenchymal stem cells, it was confirmed that MGO enhanced expression levels of osteogenic marker gene and protein than NGO [53]. Using human mesenchymal stem cells (hMSCs) and mouse embryonic stem cells, it was confirmed that integrin downstream signal involving ERK and phosphoinositide 3-kinase (PI3K) pathway was activated by graphene oxide (GO) [54-56].

hMSCs show various cellular responses and lineage specification depending on cellular nichESC such as extracellular matrix (ECM), and microenvironment through mechanotransduction [57-59]. It has been reported that physical cues such as matrix stiffness, shear stress, and cell-recognized tension surrounding stem cells can affect the lineage specification of stem cells [60-63]. In this study, using a sheet form of graphite with a diameter of more than 20 μm of precursor, the size of GO was narrowed under defined conditions to compare the effect of osteogenic differentiation and the pathways. To pursue the unity of material properties compared to GO used in previous studies, a ball-milling method that is effective in controlling the size of GO has been previously proposed [10]. The ball-milling method can reduce the size of GO particles to have a relatively tight range of particle size distribution and more polar groups than non-ball-milled GO flakes due to increased

surface area. Guided by these considerations, we propose for the first time that various size distributions of GO can affect early cell spreading and osteogenic differentiation of hMSCs through integrin receptor-subordinate signals with certain sizes of GO being effective.

Herein, pristine GO was processed through the ball-mill method. Three GO experimental groups with a relatively tight range of sizes were applied to osteogenic differentiation of hMSCs for 21 days (Figure 5.1). To analyze the mechanism involved in the osteoinductivity of GO, we focused on early cell spreading and formation of focal adhesion complex. This study contributes to bone tissue engineering as well as broadens our understanding of the correlation between osteogenic differentiation of hMSCs and graphene oxide material in terms of lateral size of GO.

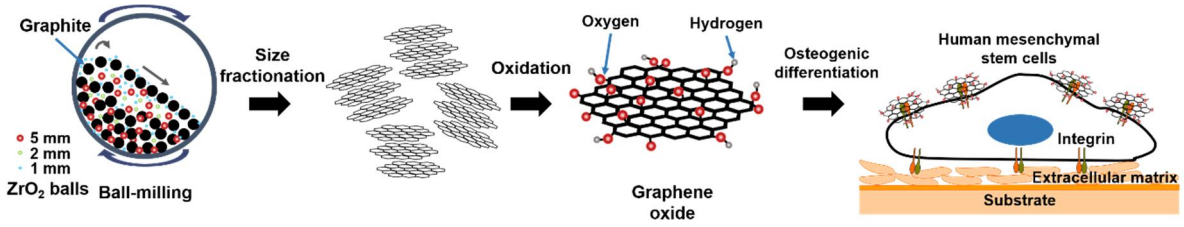

Figure 5.1. Osteogenic differentiation of hMSCs using GO flakes fabricated by ball-milling and oxidized by modified Hummers' method. Graphite was mechanically fragmentized with various sizes of zirconium oxide balls of 1, 2, and 5 mm in diameter. The fabricated powder was size-fractionated and then applied to oxidation via the modified Hummers' method, resulting in the synthesis of GO flakes with narrowly distributed sizes. Size-fractionated GO (GO-0.9, GO-1.1, GO-1.7) and no-ball-mill GO (GO-4.6) were treated with hMSCs to induce osteogenic differentiation for 21 days. The extent of osteogenic differentiation was compared between groups with different sizes of GO.

5.2. Enhancing effect of GO on osteogenic differentiation of hMSCs

To determine whether the average size of GO could affect the osteogenic differentiation of hMSCs, we examined expression levels of several osteogenic markers during osteogenesis. First, we examined gene expression levels of osteogenic markers during 21 days of osteogenic differentiation. *RUNX2*, a transcription factor essential for osteoblast commitment and early stages of osteoblast differentiation, was used to detect early osteogenic differentiation. Real-time RT-PCR analysis of early and mid-to-late osteogenic differentiation marker genes revealed significant differences of all markers in experimental groups compared to those of the control group on day 7 except for the GO-4.6 group (Fig. 5.2A). On day 14, significant differences were found for all genes except *RUNX2*, an early osteogenic marker. No significant difference was found for *RUNX2* on day 14 in the GO-4.6 group. On day 21, significant differences were found for all three osteogenic markers in GO-treated groups. Thus, all GOs used in the experiment were capable of promoting osteogenic differentiation on day 21. The difference was particularly significant in the GO-1.7 group.

Second, the activity of alkaline phosphatase was evaluated to compare the extent of early osteogenic differentiation by ALP staining (Fig. 5.2B). Activation of ALP is a representative marker of early osteogenesis. The purple color of ALP staining was remarkable in three ball-milled GO groups compared to that of the control group. The GO-4.6 group showed the least staining intensity. ARS staining results of stained minerals deposited in the extracellular matrix also showed a tendency to increase as the size of the GO sample increased except for the GO-4.6 group, similar to the gene expression profile (Fig. 5.2C). The part shown in red is a mineral. It was assessed by quantifying the stain after dissolving it with cetylpyridinium chloride and then measuring the absorbance (Fig. 5.2D). All values were normalized with the value of the control group. Results of analyzing images of bright fields revealed that the relative mineralization was the highESCt in the GO-1.7 group.

In addition, protein expression levels of type Wecollagen and osteopontin (OPN) specifically expressed in osteoblasts were compared through immunochemical analysis (Fig. 5.2E). Type

Wecollagen and OPN are both extracellular proteins expressed in the shape of an extracellular matrix [64, 65]. Consistent with previous results, ball-milled GO-treated groups showed higher protein expression than the control group. In particular, expression levels of both osteogenic marker proteins were outstanding in the GO-1.7 group. The fluorescence image was quantified and the value of relative expression level for each group was compared. It was confirmed that the GO-1.7 group showed a significant increment of type Wecollagen and OPN expression compared to all other groups (Fig. 5.2F). As such, it was confirmed that hMSCs treated with the ball-milled GO showed enhanced osteogenic differentiation compared to the control group and the GO-4.6 group, with the experimental group treated with GO with an average diameter of 1.7 μm showing the most prominent effect at 21 days after osteogenic differentiation.

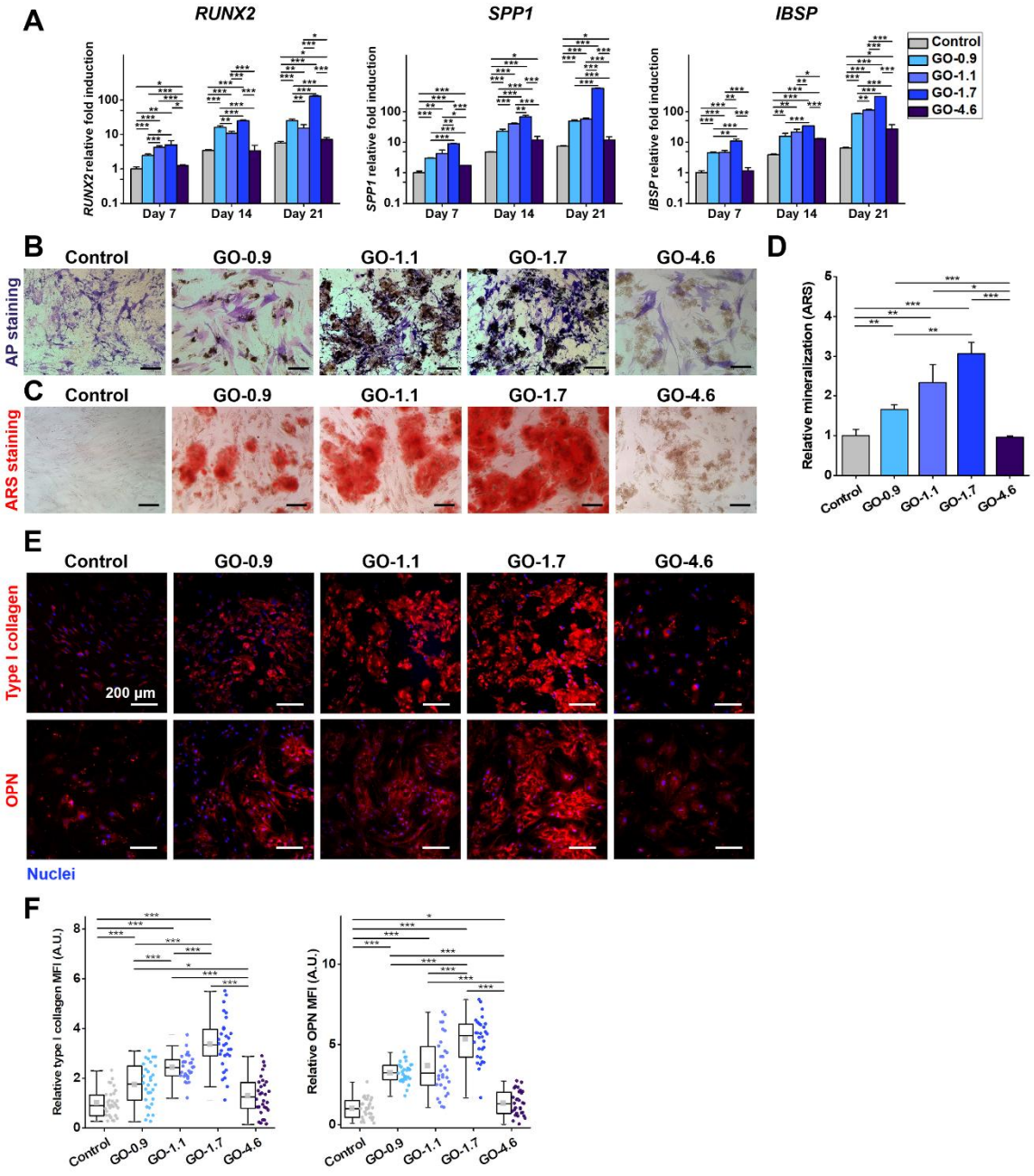

Figure 5.2. Enhancing effect of GO on hMSCs during osteogenic differentiation. (A) Relative gene expression profile of osteogenic markers for 21 days. All values were normalized against values of the control group on day 7 (n = 5). (B) Alkaline phosphatase staining for the evaluation of osteogenic differentiation of hMSCs. Cells were stained on day 21. (C) Alizarin Red S (ARS) staining for the evaluation of osteogenic differentiation of hMSCs. Cells were stained on day 21. (D) Quantitative analysis of ARS staining. All values were normalized against the control

group (n = 4). (E) Immunostaining for evaluation of osteogenic differentiation of hMSCs. Cells were stained on day 21. (F) Mean fluorescence intensity (MFI) of Type Wecollagen and OPN expressed in hMSCs. All values were normalized against the control group (n = 30).

5.3. Promotion of early cell spreading and focal adhesion complex formation of hMSCs by GO-1.7

Following previous gene expression, staining, and immunocytochemical results, experiments were conducted to understand the underlying mechanism by which the ball-milled GO, especially the GO-1.7 group, promoted osteogenic differentiation. Based on the hypothesis that the size of GO will change early mechanosensing of hMSCs, focal adhesion, a process in which cells accept physical stimuli from the surrounding environment like an extracellular matrix was investigated to assess early adhesion of hMSCs. The integrin receptor in the plasma membrane is directly bound to the RGD sequence in the extracellular matrix. Several inner proteins are directly linked to the integrin receptor to form a focal adhesion complex [4, 66]. The focal adhesion complex acts as a mediator to translate the mechanical cue received by cells through the cytoskeleton connected to the cell nucleus, thus affecting cell cycle or differentiation [67].

First, in the case of cells treated with GO, it was observed that cells stretched further than the control during the initial cell adhesion process within one day (Fig. 5.3A). Cells in the GO-1.7 group showed enhanced cell adhesion, thus enhancing cell area. Through these results, the aspect ratio (the ratio of cell area to width and height) and cell area were analyzed. As shown in the graph for each group (Fig. 4B), focal adhesion-related values of the GO-1.7 group were significantly different from those of other groups, consistent with previous results. Therefore, the accelerating effect of GO on initial cell spreading influenced the extent of osteogenic differentiation.

To evaluate the development of early focal adhesion complex, focal adhesion kinase (FAK) was labeled with red fluorescence. Values of focal adhesion area, aspect ratio, number, and mean fluorescence intensity obtained from fluorescence images were compared (Figs. 5.3C, 5.3D) [68, 69]. Similar to cell spreading results, the focal adhesion complex in ball-milled GO, especially GO-1.7, appeared sharp and edged focal adhesion complex on the image. The same tendency was also shown in quantitative comparison of FA area, aspect ratio, number, and MFI. Therefore, ball-milled GO, especially GO-1.7, showed an increase of early cell spreading caused by the initial focal

adhesion complex formation of hMSCs. The upregulation in the initial focal adhesion complex acted as a source for GO-1.7 to show a remarkable effect on osteogenic differentiation at 21 days after treatment.

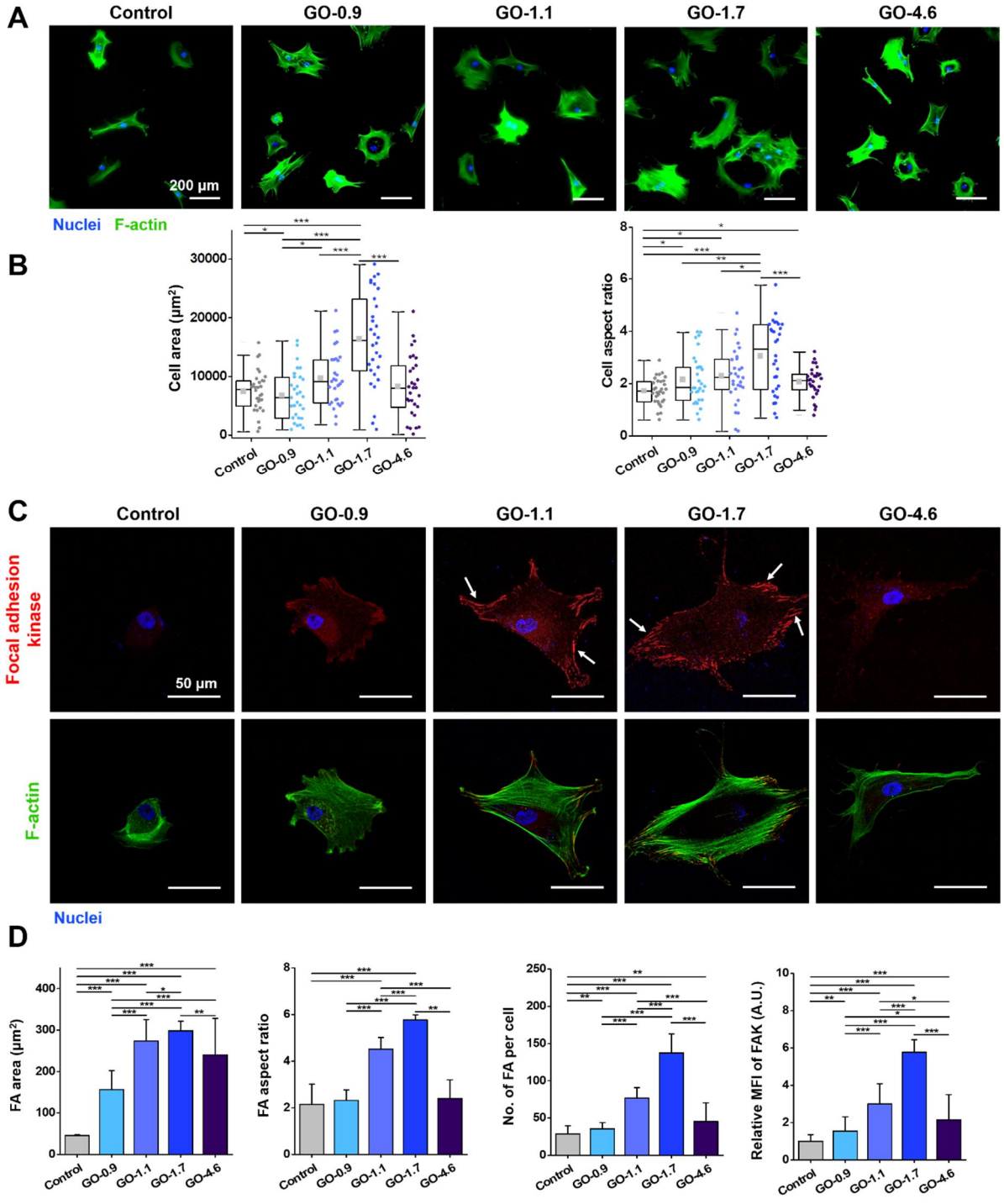

Figure 5.3. Promotion effect of GO on early cell spreading and focal adhesion complex formation of hMSCs. (A) Immunostaining for the evaluation of early cell spreading of hMSCs. In the case of GO-treated cells, it was observed that cells stretched in all directions compared to the control group during the initial cell adhesion process within one day. (B) Quantitative analysis of

early cell spreading. (n = 30). (C) Immunostaining for the evaluation of early focal adhesion formation of hMSCs. Focal adhesion kinase was labeled and analyzed. The focal adhesion complex was most developed in the GO-1.7 group. White arrows indicate the focal adhesion complex. (D) Quantitative analysis of focal adhesion. Values were obtained by analysis from the image of (C) (n = 30).

5.4. Expression and localization of osteogenic marker proteins by GO-1.7

To investigate the mechanism involved in the accelerating effect of GO-1.7 on osteogenesis of hMSCs, factors related to cell spreading were controlled by adjusting cell density. Under a confluent condition, cells were seeded six times more densely compared to the standard condition to ensure a full spread condition of hMSCs (Fig. 5.4A). The investigated cell confluency of the confluent condition was about 100% right after cell seeding. Expression levels of focal adhesion and osteogenesis-related genes, Western blot signal of the osteogenic master regulatory transcription factor, RUNX2, and YAP nuclear localization in both standard and confluent conditions of hMSCs under GO-1.7 treatment were then evaluated.

Expression levels of three genes constituting the focal adhesion complex assumed to be promoted by GO were assessed (Fig. 5.4B). As a result, when GO was used for treatment under the standard condition, it was confirmed that expression levels of focal adhesion-related genes were increased rapidly within one day of osteogenic differentiation, consistent with previous results showing that graphene oxide enhanced early cell spreading and focal adhesion of hMSCs. Expression levels of those genes were generally higher under the confluent condition than those under the standard condition without GO due to dense distribution of cellular focal adhesion structures [70]. However, under the confluent condition, there were relatively less significant differences between the two groups without or with GO, whereas significant differences in the expression level of 3 genes between the two groups without or with GO were found under the standard condition. Except for the one-star significance in *TLN* expression, there were no significant changes in *PTK2* or *PXN* expression between the two groups without or with GO under the confluent condition. These results implied that the early enhancing effect of GO on cell spreading and focal adhesion did not appear in the confluent condition, a situation where cell spreading had already been sufficiently achieved by other environmental components.

As an extension, expression levels of *RUNX2*, an early osteogenesis-related gene, showed a tendency similar to those of focal adhesion-related genes under standard and confluent conditions

(Fig. 5.4C). These results support previous findings that an increase in initial focal adhesion can lead to an increase in early osteogenic differentiation-related signals [71]. As a result of Western blot analysis for the expression of RUNX2 protein, the effect of GO in promoting osteogenic differentiation was observed in both standard and confluent conditions, consistent with previous results in terms of GO presence (Fig. 5.4D). However, the overall expression of RUNX2 protein in each group was decreased in the confluent condition. These results revealed that the *RUNX2* gene was upregulated. However, due to factors such as influences of the interplay of YAP protein acting as a down-regulator of early osteogenesis, *RUNX2* seemed to have a barrier to reaching sufficient protein expression level in the confluent condition than in the standard condition [72, 73].

Gene expression levels of *YAP* during the initial osteogenic differentiation process due to mechanosensing were evaluated. Results are shown in Fig. 5.4C. Expression levels of *YAP* were increased in GO groups under both standard and confluent conditions compared to those in the group without GO treatment. The overall expression level of *YAP* under the confluent condition was less than that under the standard condition. To compare images stained with cytoskeleton and nucleus markers, nuclear and cytosol expression levels of the YAP protein shown in green and nuclear localization level of YAP based on ICC images were quantified (Figs. 5.4E, 5.4F). The nuclear localization of YAP protein was significantly increased in the group treated with GO under the standard condition, whereas it was decreased in both two groups (without or with GO) under the confluent condition. Contrary to gene expression results, there was no significant difference in the level of nuclear localization between the two groups (without or with GO) under the confluent condition. These results are consistent with a previous report showing that nuclear localization of YAP is decreased instead of an increment of N-cadherin expression in the maximized cell-to-cell junction environment [68]. Similar to the expression tendency of RUNX2, it was observed that the ability of GO to promote early osteogenic differentiation was not noticeable in the confluent environment where cell-to-cell interaction was maximized. These results demonstrate that GO can promote early osteogenic differentiation of hMSCs by FAK-subordinate pathways, leading to initial

cell spreading, increment in nuclear localization of YAP, and then upregulation of osteogenic master regulatory transcription factor RUNX2 expression in this study.

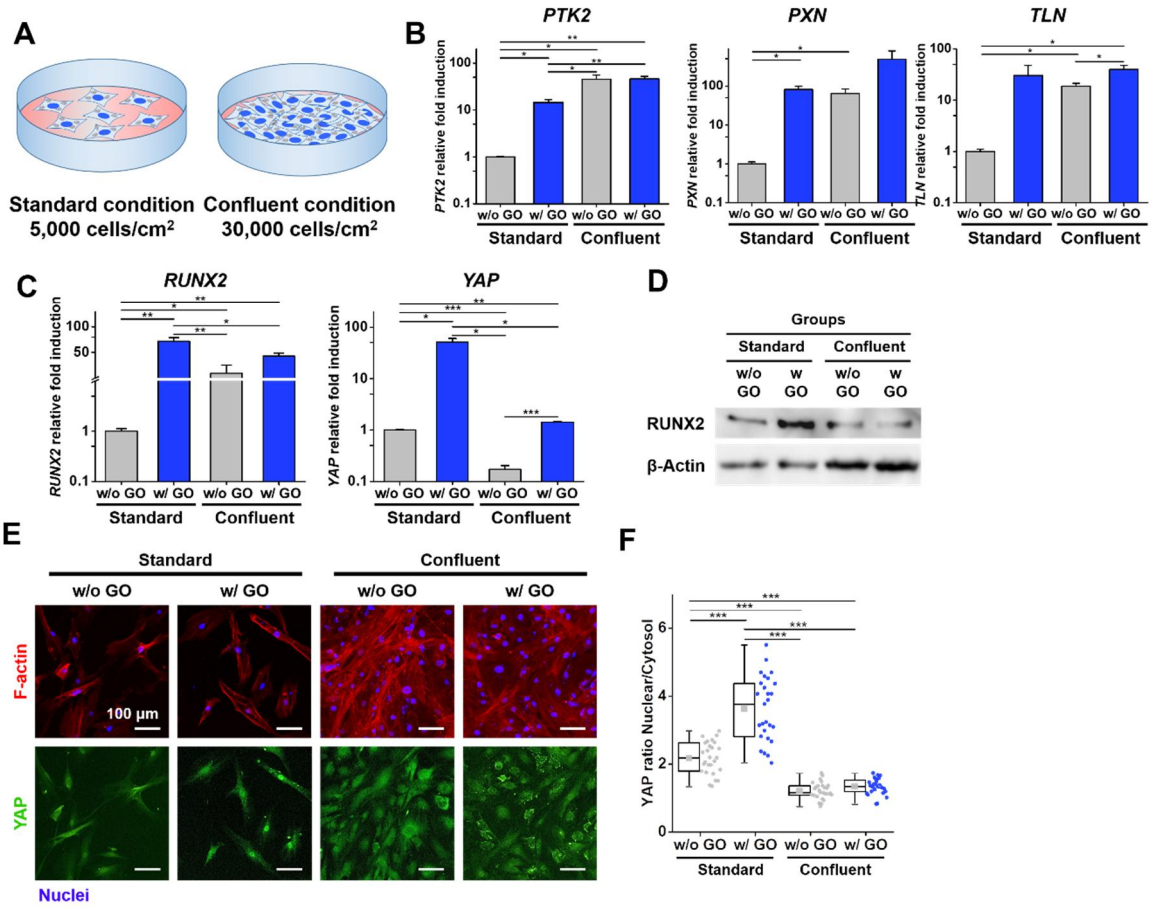

Figure 5.4. Effect of GO on the expression and localization of osteogenic marker proteins.

(A) Schematic design for the evaluation of difference between standard condition and confluent condition. (B) Relative gene expression of focal adhesion-related genes on day 1 (n = 3). (C) Relative gene expression of osteogenesis-related genes on day 1 (n = 3). (D) Western blotting of RUNX2 protein. (E) Immunostaining of YAP protein for the evaluation of nuclear localization. (F) Quantification of intranuclear localization of YAP protein. Values were obtained by analyzing images in (E) (n = 27).

5.5. Proposed mechanism of osteogenic differentiation enhanced by GO

To ascertain if the variation in the expression level of the early focal adhesion complex protein influenced osteogenic differentiation when hMSCs were treated with GO, the expression of signal producer proteins involved in the mechanotransduction pathway was examined by Western blot (Fig. 5.5A). As representative kinases that might stimulate the focal adhesion signal to osteogenesis-related signal, the expression and phosphorylation of FAK, mitogen-activated protein kinase (MEK), and extracellular signal-regulated kinase (ERK) were examined [74, 75]. When FAK, MEK, and ERK phosphorylation levels were evaluated, it was found that GO groups—especially the GO-1.7 group—had greater levels than the control group. This finding is in line with earlier findings from this study that showed improved osteogenic differentiation.

The proposed signaling pathway is shown in Fig. 5.5B. First, the expression and phosphorylation of FAK protein belonging to the focal adhesion complex were increased. Phosphorylation levels of downstream kinases MEK and ERK were also increased. Thus, the pathway leading to osteogenic differentiation was confirmed. The increase in the expression of RUNX2 was shown in the Western blot result (Fig. 5D, Fig. S4) for the GO-1.7 group. By affecting local adhesion formation, cytoskeletal mechanics, and ERK pathways, mechanical sensing promotes stem cell differentiation [76]. Elongated cell shape causes cytoskeletal stress, which activates FAK in osteogenic differentiation-mediated pathways. Additionally, FAK activation that results in positive feedback boosts cytoskeletal tension and encourages osteogenic differentiation. According to earlier research, proteins in the cell membrane interact with functional groups on the basolateral and marginal surfaces of GO, such as epoxide, carboxyl, and hydroxyl groups, in order to bind to the compound [77, 78].To favorably control osteogenic development, activated FAK is autophosphorylated, and subsequent ERK signaling pathways provide mechanistic data to the cell nucleus [79]. In this work, it was established that GO itself, rather than the action of proteins or growth factors localized to GO, promoted spreading in the early cell adhesion phase within 1 day. For the first time, we show that

during the early stage of cell attachment, these physical stimuli act as a trigger and intrinsically enhance the integrin signal to induce osteogenic differentiation.

Among GO groups of different average sizes obtained through ball-mill method, we found that GO-1.7 had a remarkable effect in promoting osteogenic differentiation. In stem cell research using graphene-based materials, various studies have been conducted on the impact of physicochemical properties such as lateral size of GO and functional group modification through surface functionalization on cytotoxicity and lineage specification of stem cells [50, 80, 81].

The level of reactive oxygen species (ROS) might be a factor that affects the osteogenic differentiation of hMSCs [82]. According to a previous study, the presence of GO can reduce the ROS level. Thus, each group was investigated in the present study. It was confirmed that the ROS level was decreased consistently in GO-treated groups than in the control (Fig. 5.6). These factors might have also enhanced osteogenic differentiation. Also, one limitation of our study is that all experiments were performed *in vitro*. According to previous work, the *in vivo* experiment employing a biocompatible scaffold including GO could clarify whether GO could accelerate regeneration of bone defect model owing to increased angiogenesis [83]. Assessment of TEM and SEM images obtained in this study has some limitations due to sample deformation such as severe dehydration during sample fixation and resin fabrication for live imaging and analysis of detailed interactions between cells and GO. In addition, fluorescence imaging of GO on the cellular surface using Dil staining might be an option for distinguishing the presence of GO on the cell surface. However, a method for imaging or analyzing detailed physicochemical interactions between the cellular membrane and oxidative functional groups in GO needs to be developed [84].

Previous studies have shown that the size of GO sheets affects both cytotoxicity and the determination of stem cell lineages [50]. For instance, it has been shown that GO substrate with a micron size range of 1–10 μm was more effective than GO with a nano-size range in promoting osteogenic differentiation or neuronal differentiation [53]. In this study, the effect of a specific size of micro-sized GO on osteogenic differentiation of hMSCs was observed using three

GO groups with relatively uniform size distribution and GO groups without size control. It was confirmed that a specific GO group exhibited enhanced osteogenic differentiation. The optimal average size was found to be 1.7 μm. Through these findings, it can be inferred that there would be a particular size of GO that could be attached to the cellular membrane in order to change the cellular mechanosensing in relation to the curvature of cellular membrane.

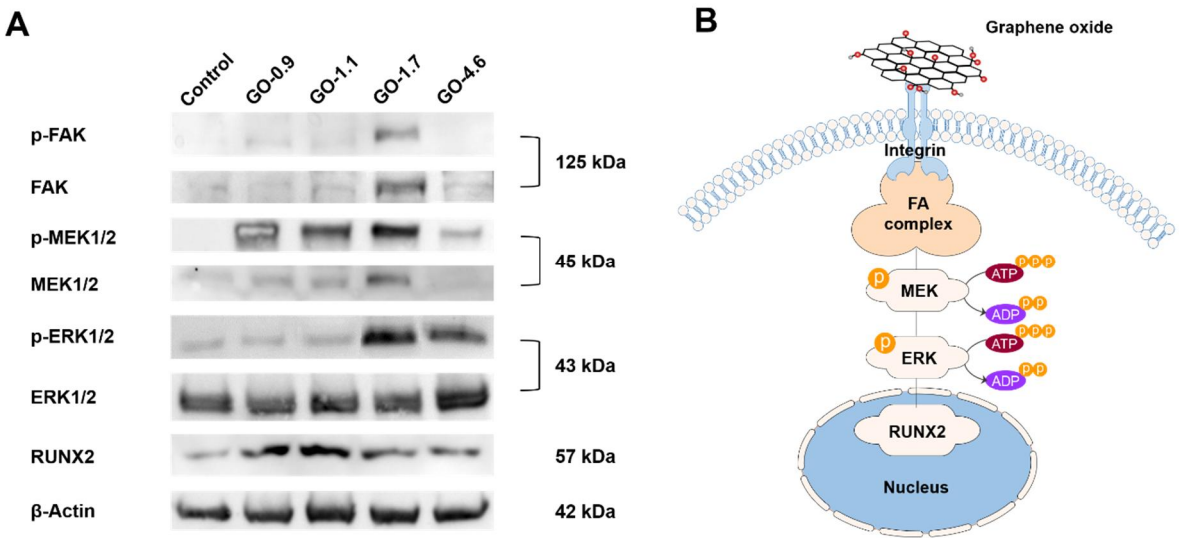

Figure 5.5. Signaling pathway of osteogenic differentiation enhanced by GO. (A) Western blotting of focal adhesion-related signaling proteins. Higher expression was observed in GO groups (especially the GO-1.7 group) than in the control group. (B) Proposed mechanism of GO. Focal adhesion stimulation by attachment of GO on the cellular surface of hMSCs exerted an osteogenic differentiation function following downstream signals.

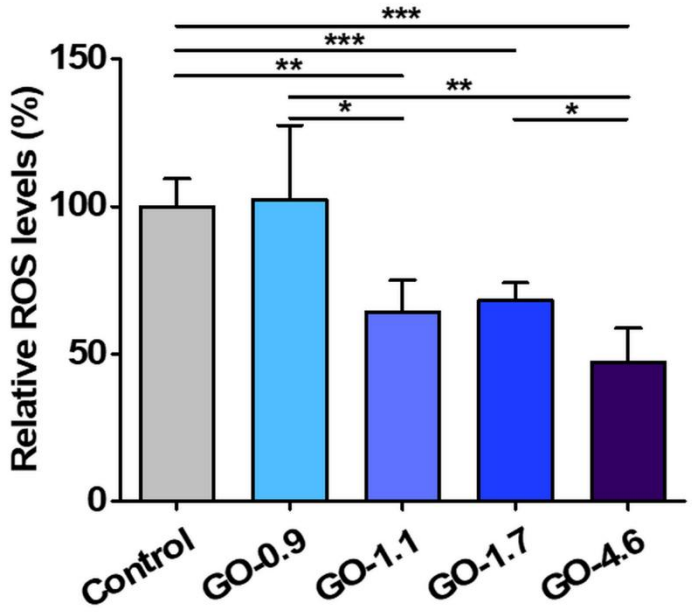

Figure 5.6. Amount of relative oxygen species (ROS) of hMSCs treated with GO. The amount of ROS is expressed in green fluorescence using an ROS detection kit. Measurements were performed for each experimental group, including positive and negative controls. Result is shown in the amount of ROS in each experimental group as a percentage with the control set to 100%. Except for the GO-0.9 experimental group which had a large deviation, obtained results were almost similar to the control group. The amount of ROS generated was significantly reduced in all other experimental groups. These results indicate that GO is involved in the mechanism of ROS reduction as previously known. This might promote antioxidative reaction and osteogenic differentiation.

5.6. Conclusions

In this study, the pristine graphite was processed through a ball-mill method known as an effective GO size fractionation method. The obtained three GO samples with narrower size distribution were applied to osteogenic differentiation of hMSCs for 21 days. Gene expression levels, ALP activity, calcification, and protein levels were determined at 21 days after osteogenic differentiation for the control group not treated with GO (GO-4.6) and the three groups treated with GO-0.9, GO-1.1, GO-1.7. In the GO-treated experimental group, osteogenic differentiation was generally improved, with the GO-1.7 group showing the most prominent results. To analyze the cause of this osteogenic differentiation promoting effect, the fact that GO promoted early cell spreading and the formation of focal adhesion complex was investigated. A tendency to increase focal adhesion was observed, similar to that of osteogenic differentiation. As a result of analyzing the underlying mechanism through Western blot and YAP nuclear localization, it was confirmed that cellular mechanosensing was enhanced by GO, especially by GO-1.7, thus promoting osteogenic differentiation. The significance of this study was that effects of various lateral sizes of GO on mechanosensing of hMSC were evaluated. Detailed interactions between cells and GO need to be assessed in subsequent studies. This study contributes to our understanding of the physicochemical effect of graphene material on hMSCs and attributes for tissue engineering research by increasing the efficiency of osteogenic differentiation.

Chapter 6

Enhancing effect of graphene oxide flakes on stem cell viability in single-cell detachment and shear stress-caused apoptotic circumstances

Chapter 6. Enhancing effect of graphene oxide flakes on stem cell viability in single-cell detachment and shear stress-caused apoptotic circumstances

6.1. Introduction

The utility of stem cell therapeutics is limited due to the low cell engraftment rate and apoptosis called anoikis at the transplantation site (Fig. 6.1A). Graphene oxide can interact with proteins like integrin on the cellular membrane through its versatile oxidative group, and it has been known in previous studies that it can be applied for the regulation of stem cell behavior by various cellular responses like mechanosensing [85]. In this study, graphene oxide was used as a cellular adhesive to increase cell viability *in vitro* environment that simulates single-cell detachment and physiological shear stress of the transplantation site (Fig. 6.1B). It was confirmed through Live/Dead assay and CCK8 assay that the hMSCs and hESCs treated with GO under non-adhesive coating with pluronic F-127 and shear stress through shaking incubator showed higher survival rates and larger cellular area. The effect of enhanced viability was more pronounced in the hESCs. Also, it is known that the lateral size of GO is an important factor in stem cell viability and differentiation, and it was confirmed that the GO experimental group with an average diameter of 1.7 μm had greater cell viability enhancing effect than the GO with a diameter of 4.6 μm. It was confirmed that micro-sized GO was attached to the cell surface and functions as a cell adhesion agent in a non-adhesive environment. These results show that GO is a material that can be used for stem cell transplantation to increase the engraftment rate of cells [84].

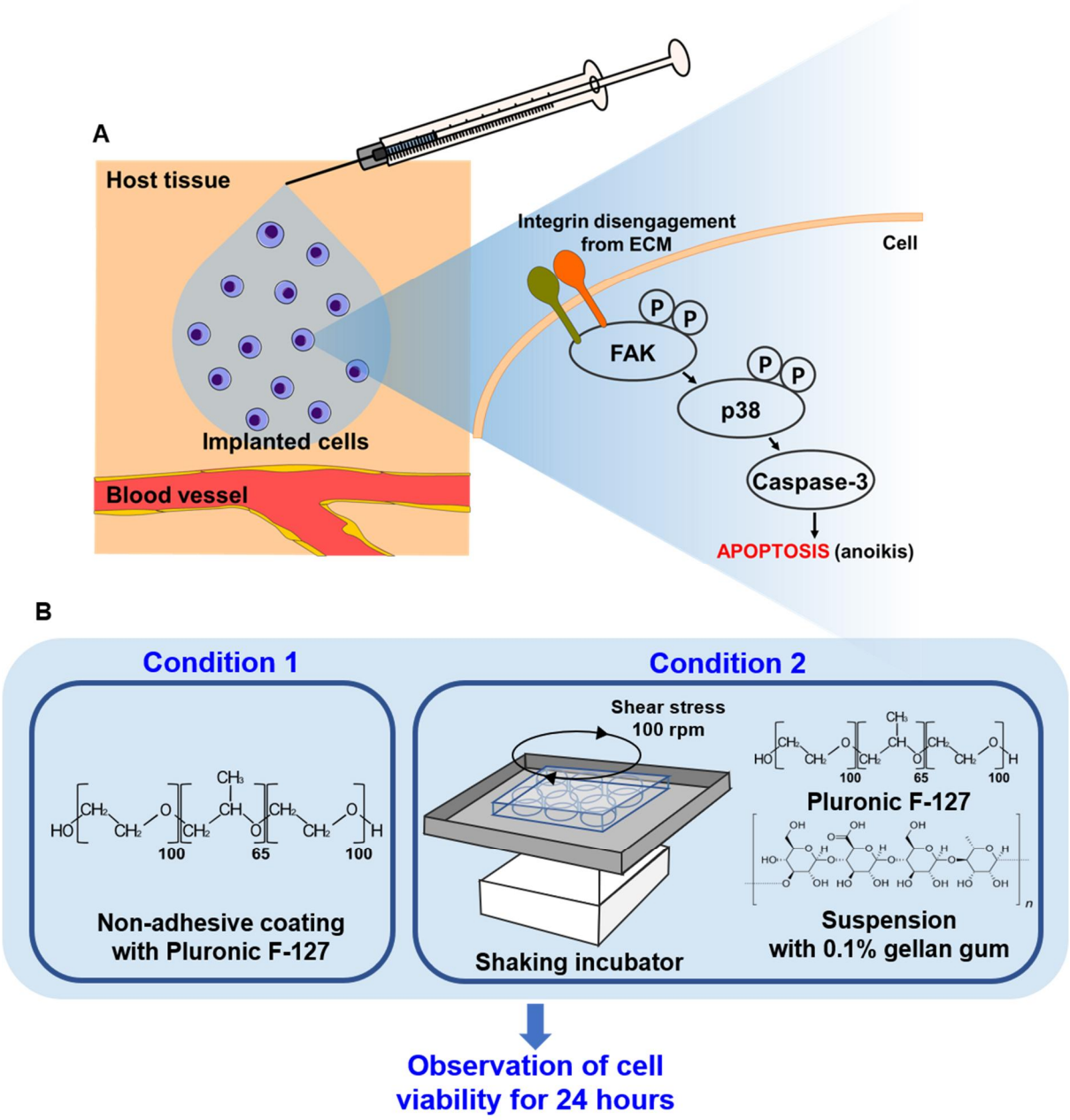

Figure 6.1. Research objective and schemes. (A) Anoikis in transplantation site (B) In vitro research scheme

The research to lower apoptosis in single cell detachment culture by GO by mimicking cell transplanting and utilizing the impact of boosting cell focal adhesion by go. This study was based on the findings of the previous chapter. It can be used to suspension culture or cell transplantation to boost cell viability. It was attempted to lessen the apoptosis that happens during cell transplantation therapy using these characteristics of GO. The poor engraftment rate of the transplanted cells necessarily restricts research on the transplantation of stem cells into regions needing regenerative therapy [86]. In order to address this issue, GO was employed as a substance to boost the survivability of the cell in both the in vitro environment, which mimics the shear stress of the real environment, and the single cell detachment condition, which illustrates the transplant site.

6.2. Viability of hMSCs treated with GO-1.7 in non-adhesive condition and shear stress

First, in condition 1, Pluronic F-127 coating used for general non-adhesive coating was used.

when comparing cell survival through live/dead assay at 4 hour intervals up to 24 hours, at 24 h, cell survival was significantly increased during go treatment than control, and even though non-coating treatment was performed, the experimental group treated with GO was somewhat on the floor (Fig. 6.2A, B). It has been confirmed that adhesion is possible.

Comparing this through image analysis, it was confirmed that when treated with GO compared to control, cells were killed except for 20% in control, but maintained about 50% survival. Some adherent cells were observed in hMSCs treated with GO-1.7 while control cells remained round-shape because of non-adhesive coating with Pluronic F-127. This effect was confirmed by CCK8 assay, which remained different in the two groups until 48 hours, and when the cell size was compared at 24 hours, it was confirmed that the cells treated with GO expanded their cell area through some adhesion (Fig. 6.2C, D).

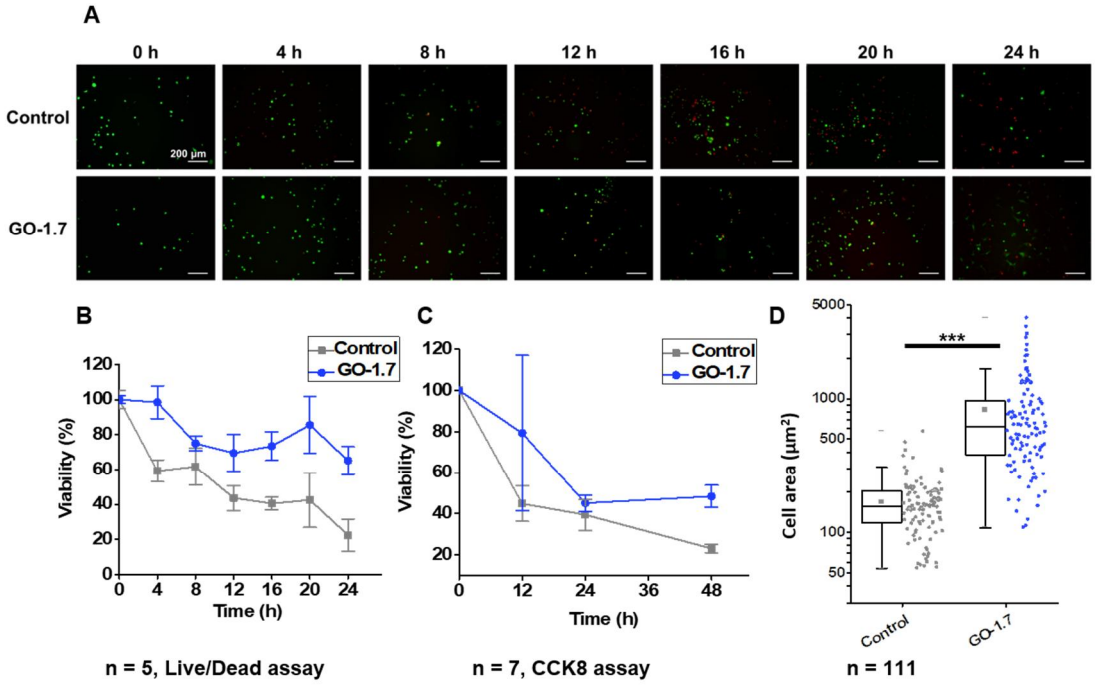

Figure 6.2.Viability and cell area of hMSCs treated GO-1.7 during 24 hours in non-adhesive condition (condition 1). (A) Live/Dead assay of hMSCs treated 1.7 μm-GO during 24 hours. Cells were observed every 4 hours. (green: live cells, red: dead cells) (B) Viability of hMSCs analyzed by Live/Dead assay until 24 hours. (n = 5) (C) Viability of hMSCs analyzed by CCK8 assay until 48 hours. (n = 7) (D) Comparison of cell area between two groups. (n = 111)

Second, it was tried to compare the cell survival effect of GO by creating an environment where shear stress is applied through a shaking incubator. Similarly, compared through image analysis, when treated with GO compared to control, the cells had a higher survival rate in GO-1.7 than in control and GO-4.6, which showed a greater difference when confirmed by CCK8 assay up to 48 hours (Fig. 6.3A, B). When the cell size was compared at 24h, the area of cells thought to have activated focal adhesion to some extent by treatment with GO-1.7 increased slightly, but because adhesion did not occur as in condition 1, it was not very large with the control (Fig. 6.3C, D). showed the difference. In the case of GO-4.6, its cytotoxicity is also somewhat higher than that of GO-1.7. In particular, in the results of previous studies, there was no effect to activate focal adhesion, so it did not enhance cell survival.

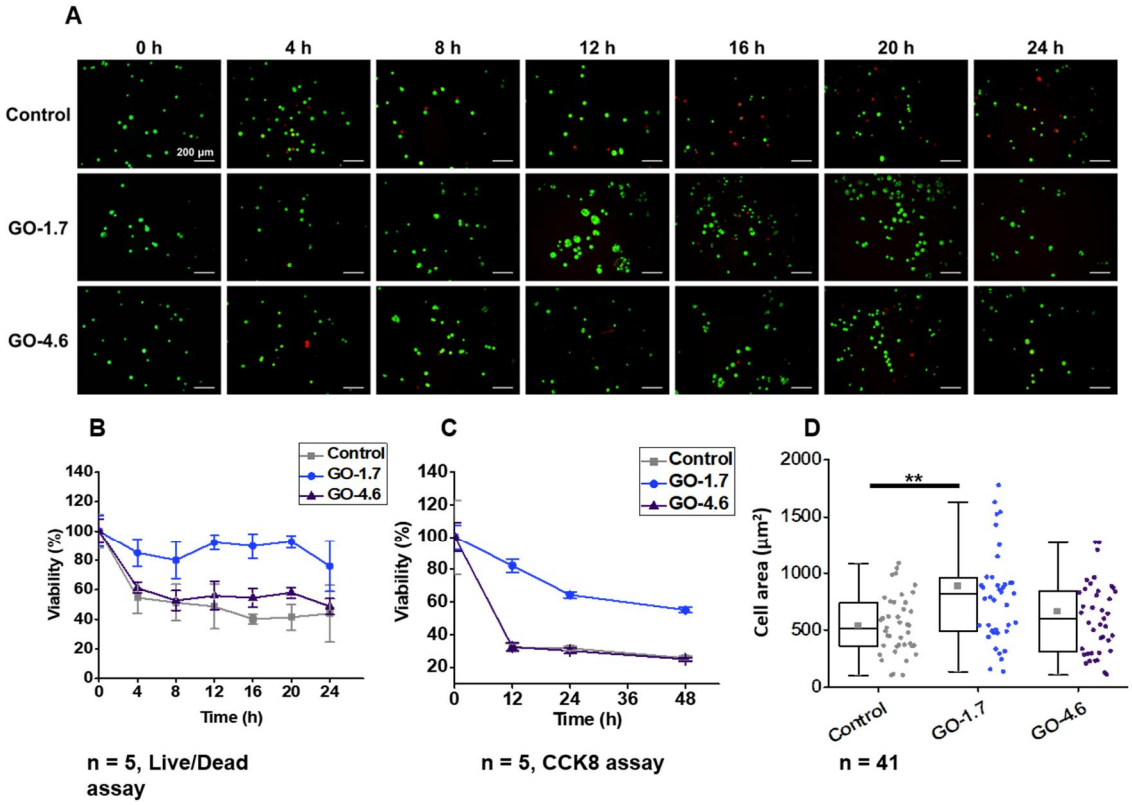

Figure 6.3. Viability and cell area of hMSCs treated GO-1.7 and GO-4.6 during 24 hours in non-adhesive condition with shear stress (condition 2). (A) Live/Dead assay of hMSCs treated GO-1.7 and GO-4.6 during 24 hours. (B) Viability of hMSCs analyzed by Live/Dead assay until 24 hours. (n = 5) (C) Viability of hMSCs analyzed by CCK8 assay until 48 hours. (n = 5) (D) Comparison of cell area between three groups. (n = 41)

6.3. Viability of hESCs treated with size-controlled GO flakes in non-adhesive condition

Human eembryonic stem cells are vulnerable to apoptosis during cell separation and dissociation. They undergo massive apoptosis, particularly after complete dissociation, and the replication efficiency of dissociated hESCs is usually less than 1% after 1 day.

As a result of observing hESCs in a non-adhesive environment for 24 h, it was confirmed that the survival rate was higher in the size-controlled GO test group, compared to the death of most cells in the two experimental groups (Fig. 6.4A, B). It is noteworthy that, unlike hMSC, hES had an increased survival rate when treated with GO-0.9. It is speculated that the size of hES cells itself is smaller than that of hMSCs, which may have changed the surface area outside the cell and the degree of mechanosensing by the size of GO. In particular, it is known that the survival rate can be increased from 1% to 26-30% through rock inhibitors, which are commonly used to reduce apoptosis of HES. can be checked.As such, it was confirmed that the experimental group treated with size-controlled GO showed a higher survival rate in an environment where adhesion was prevented. In addition, the lateral size of GO is known to be an important factor in stem cell response [48]. In particular, in this experiment, the sub-signal of the focal adhesion complex through integrin was activated, so that the average diameter of hMSCs was GO-1.7 and hES, GO-0.9. It has been confirmed that the effect of improving cell viability is high. These results show that GO is a material that can be used for stem cell transplantation to increase the engraftment rate of cells.

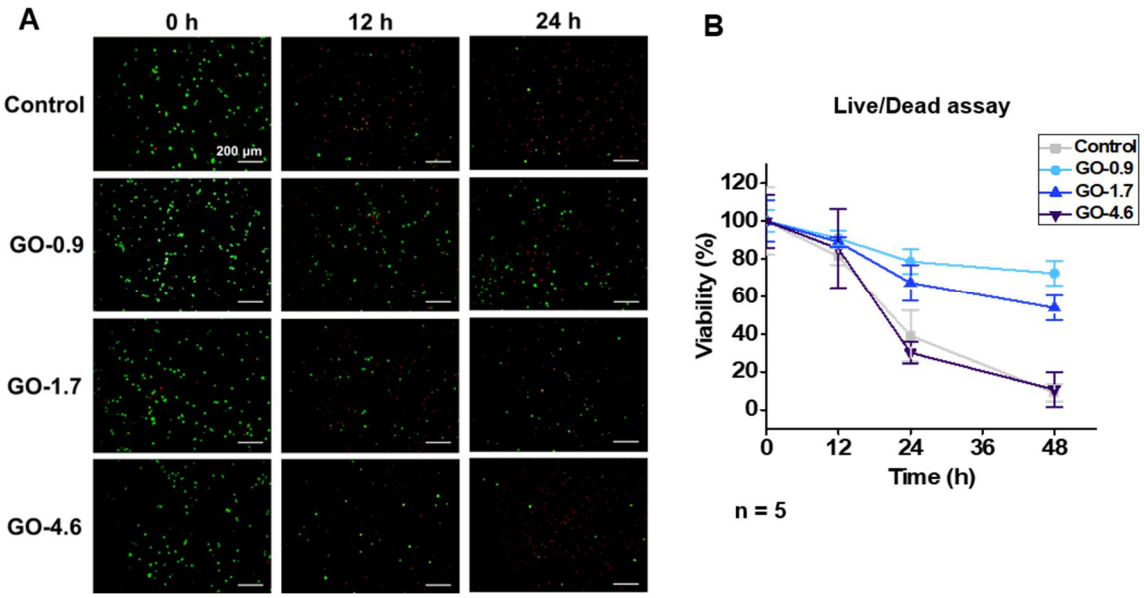

Figure 6.4. Viability of hESCs treated 3 GO groups during 24 hours in non-adhesive condition (condition 1). (A) Live/Dead assay of hESCs treated GO groups during 24 hours. (B) Viability of hESCs analyzed by Live/Dead assay until 24 hours. (n = 5)

6.4. Conclusions

hMSCs treated with GO-1.7 showed enhanced cell viability in the control group in non-adhesive conditions. hMSCs treated with GO-1.7 in non-adhesive, shear stress condition showed enhanced cell viability than the control and GO-4.6 treated group. In the case of hESCs, there was an effect of enhancing cell activity in the GO-0.9 group. As a result, GO-1.7 and GO-0.9 played as a cellular adhesive, resulting in increased cell size and increased cell survival rate in harsh conditions in hMSCs and hESCs, respectively. These properties of GO can be utilized to increase the cell viability at the transplantation site (Fig. 6.5).

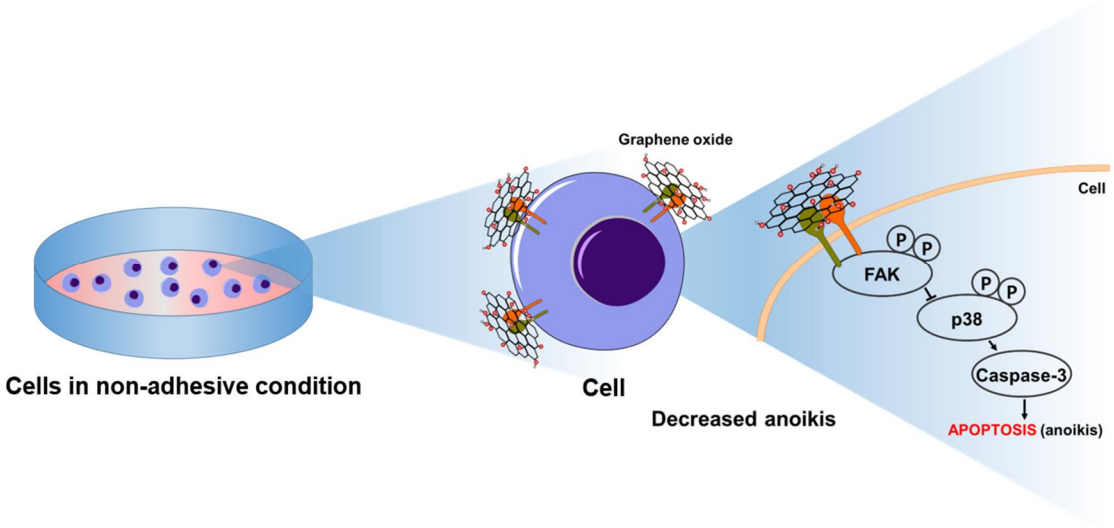

Figure 6.5. Decreased deterioration of cells on non-adhesive condition through the effect of size-controlled GO.

Chapter 7

Enhanced neural differentiation of adipose-derived human mesenchymal stem cells using size-controlled graphene oxide flakes

Chapter 7. Enhanced neural differentiation of adipose-derived human mesenchymal stem cells using size-controlled graphene oxide flakes

7.1. Introduction

In autologous cell transplantation and tissue engineering researches to treat various neuronal disorders, efforts to develop an efficient platform for stem cell growth and neural differentiation are needed [87]. Recently, it has been reported that monolayer graphene oxide enhanced neural differentiation by regulating cell-cell and cell-substrate interactions and thereby promoting outgrowth of neurites [88]. Herein, cell-penetrating magnetic nanoparticles (MNPs) and monolayer graphene oxide sheets were utilized to form adipose-derived human mesenchymal stem cells (ADSCs) spheroids and neural differentiation was analyzed. Through intracellular delivery of MNPs into the ADSCs and treat of graphene oxide sheets, suspended and magnetized ADSCs efficiently clustered into spheroids containing graphene oxide driven by magnetic pin-based external magnetic forces. After five days of neural differentiation, increment of nissl bodies was observed by nissl staining in the spheroid group. Also, expression of PAX6 (paired box 6) and Tuj1 (class III beta tubulin), neuronal marker protein, was demonstrated only in the spheroid group by immunocytochemistry as well as neural induction marker genes; NES (nestin), TUBB3 (class III beta tubulin), GFAP (glial fibrillary acidic protein) [89].

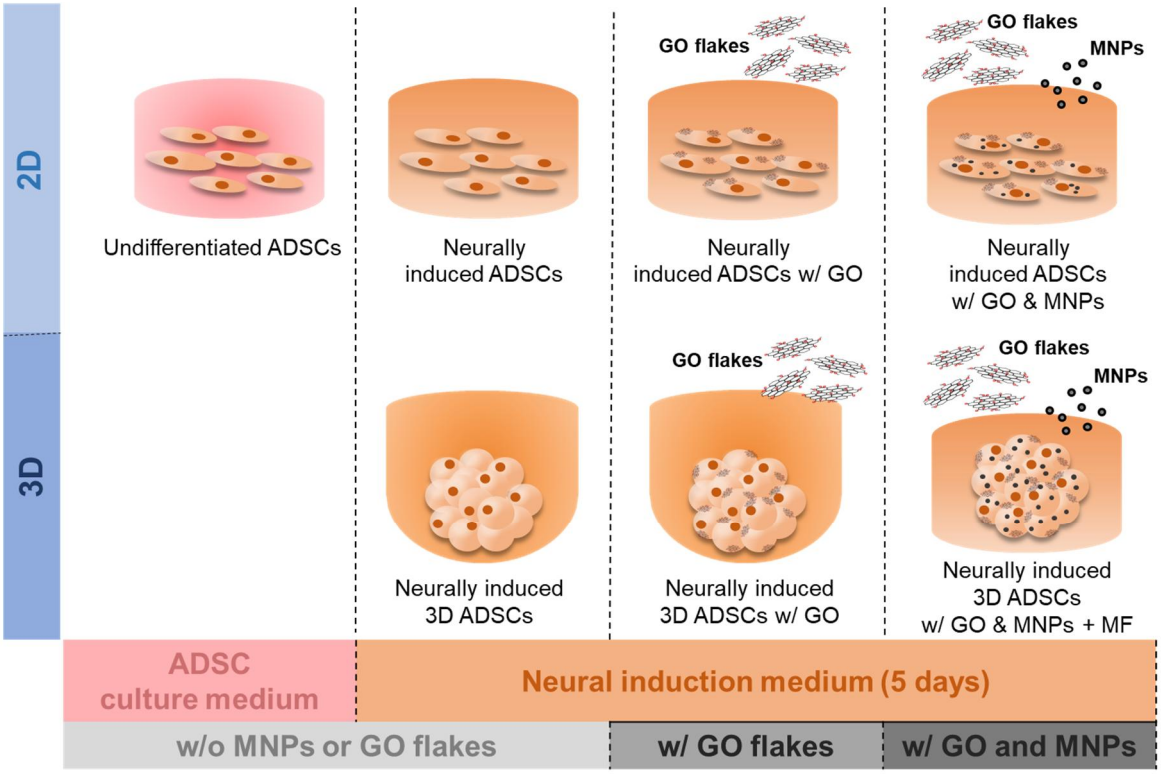

Figure 7.1. Schematic for experimental groups.

7.2. 3D culture of ADSCs

When magnetic nanoparticles are introduced into mesenchymal stem cells and cultured in two dimensions, there is no significant difference from the conventional culture without magnetic nanoparticles. Attached to the bottom, the mesenchymal stem cells were cultured while maintaining their original shape, and showed a tendency to gradually proliferate. The mesenchymal stem cells cultured two-dimensionally on a flasks were observed to be attached in a star-shaped form.

Cells into which magnetic nanoparticles are introduced are magnetized and have mobility by magnetic force. Therefore, it is easy to control the movement by external magnetic force after introducing magnetic nanoparticles into the cell to realize the three-dimensional mesenchymal stem cells. It was confirmed that graphene was attached to the outer part of the cell membrane and aggregated, which could be observed under a microscope. As the magnetized cells were removed from the flask and injected on the magnetic force concentration platform, it was observed that the cells gathered to a single point as shown (Fig. 7.2A). The magnetic force concentrated by the tack was enough to attract the cells magnetized by the magnetic nanoparticles, so the cells gathered together to form a three-dimensional shape in space.

Responses in cell viability of ADSCs depending to MNP and GO concentrations were compared (Fig. 7.2B, C). Cosnistent with the previous results, MNPs themselves did not cause significant cytotoxicity, and GO showed toxicity with increased concentration. The experiment was conducted at a concentration of 10 μg/ml with relatively low toxicity.

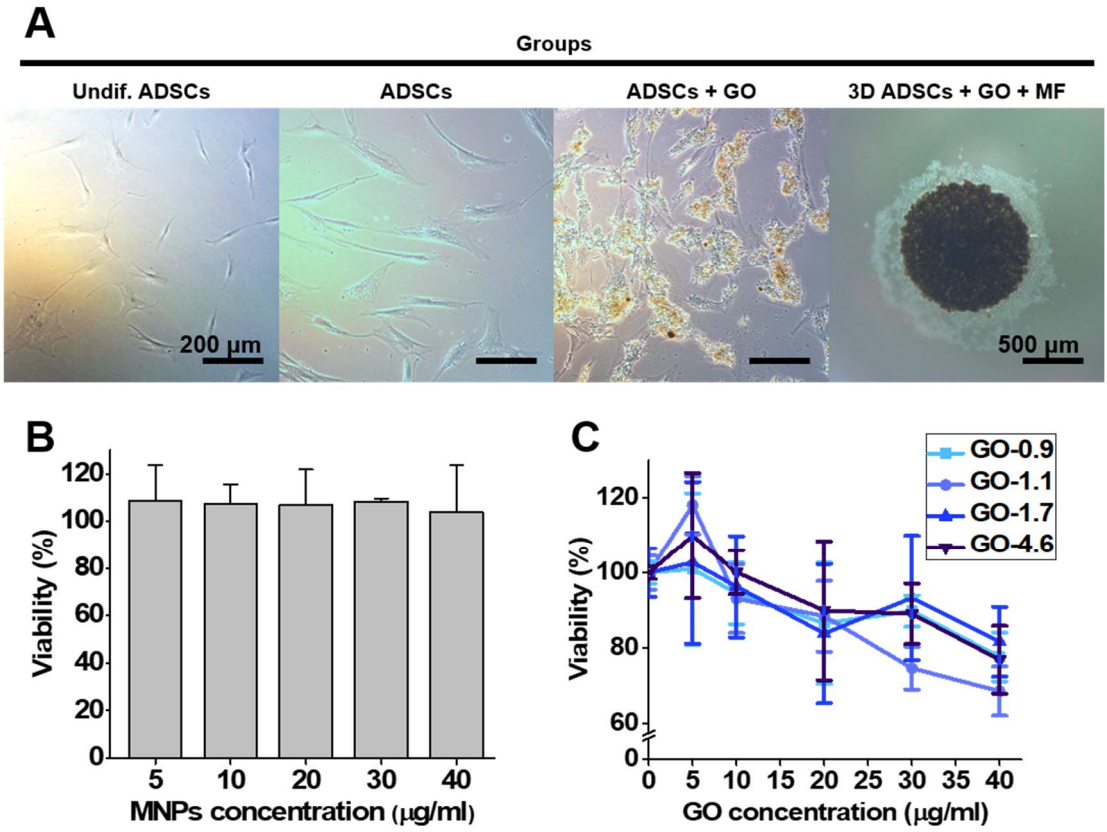

Figure 7.2. Morphology and dose-dependent viability of ADSCs in response of GO and MNPs. (A) Optical images of experimental groups. (B) MNPs and GO dose-dependent viability of ADSCs measured with CCK8 assay.

7.3. Gene expression of neural induction markers in ADSCs

To determine whether the average size of GO could affect the neural differentiation of hADSCs, we examined expression levels of several neurogenic markers during neurogenesis. First, we examined gene expression levels of osteogenic markers during 5 days of neurogenic differentiation. *NES*, a a cytoskeletal intermediate filament initially characterized in neural stem cells, was used to detect early neural differentiation in Fig. 7.3A [90]. Real-time RT-PCR analysis of other neurogenic differentiation marker genes, *TUBB3* and *GFAP* revealed significant differences of all markers in 3D ADSCs groups compared to the 2D ADSCs group (Fig. 7.3B, C). On day 5, significant differences were found for all genes. Thus, all GOs used in the experiment were capable of promoting neural differentiation on day 5 in 3D culture condition. The difference was particularly significant in the GO-0.9 group in 3D condition.

When compared in the two-dimensional experimental group, it was confirmed that the neural differentiation of ADSCs was slightly promoted by GO, as previously known. In addition, since it was previously confirmed that MNPs also had a neuronal differentiation-promoting effect, the neural differentiation-promoting effect was observed in the group to which MNPs were added accordingly [91]. At this time, the neural differentiation promoting effect of the two-dimensional experimental group was similar to the bone differentiation promoting effect, and the result was dependent on the size of GO. In particular, it was confirmed that the GO-1.7 experimental group showed a slightly more accelerated neural differentiation effect than other groups. On the other hand, GO-4.6 did not show a significant difference compared to the existing method without introducing MNPs in the expression of NES and TUBB3, confirming that it follows a similar trend to the previous results.

In the case of the 3D experimental group, interesting results were confirmed. Compared with the 3D ADSCs w/o GO experimental group, the 3D experimental group using GO and magnetic force showed high neuronal differentiation efficiency, respectively. However, the effect of GO size

was quite different from that of 2D. At this time, it was confirmed that neural differentiation was most promoted in the GO-0.9 experimental group, not GO-1.7.

As a result, the optimal GO size to promote neuronal differentiation is different between the two-dimensional culture environment and the three-dimensional culture environment, because the optimal GO size to promote cell-to-cell interaction is different in the culture environment.

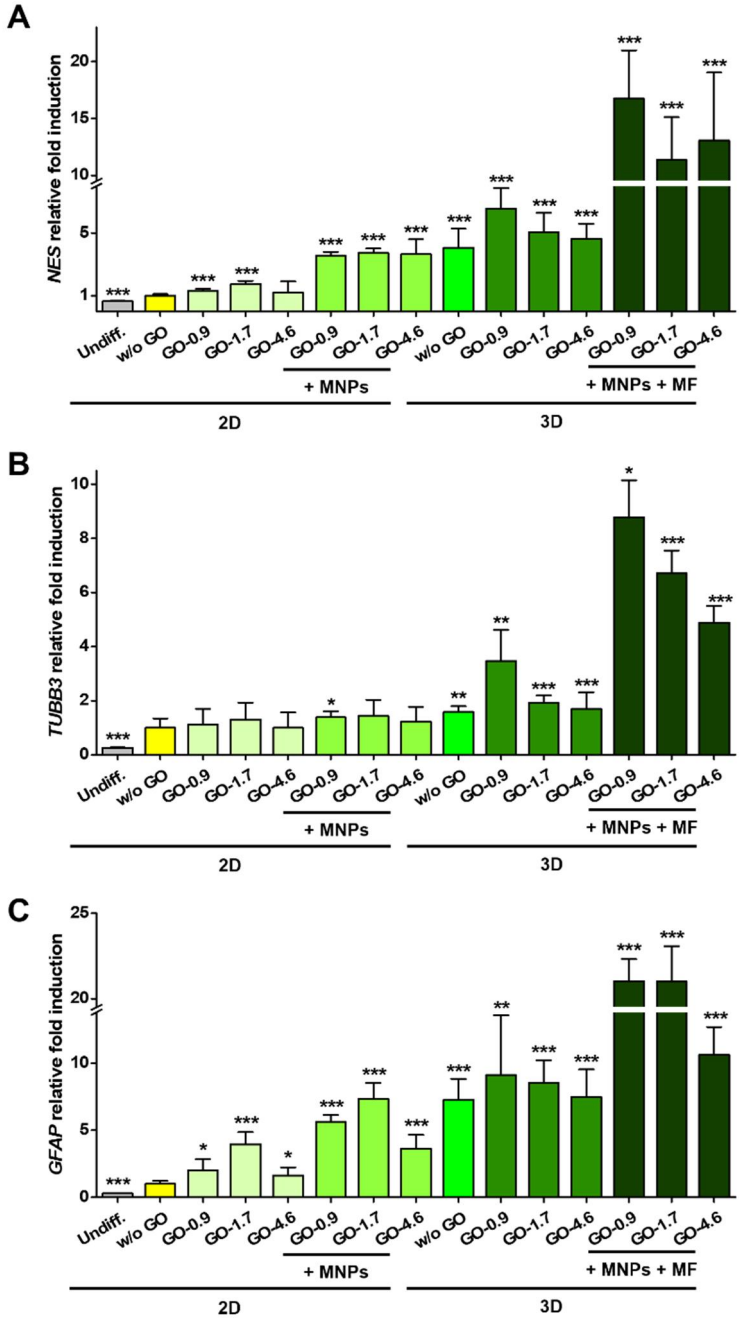

Figure 7.3. Relative mRNA expression level of neural induction markers for 5 days of neural differentiation on ADSCs. (A) NES (B) TUBB3 (C) GFAP (n = 7 for each markers). GAPDH was used as housekeeping gene. P values were compared with 2D w/o GO group for each experimental group.

7.4. Expression of neural induction markers in ADSCs

Mesenchymal stem cells cultured in two and three dimensions and induced to differentiate into neural tissue cells by the neural differentiation medium were observed. In the three-dimensionally implemented mesenchymal stem cell experimental group, it was cultured in a three-dimensional form for one week, and in a two-dimensional form for one week, induced to form a form that can be sufficiently attached to the floor.

The expression of PAX6 and Tuj1, a neural marker protein, was confirmed at the protein level in more detail through immunochemical staining (Fig. 7.4A-C). PAX6 is a protein expressed when differentiation into ectoderm stems occurs during embryonic development [92]. Compared to the previous control groups, PAX6 and Tuj1 was observed as green fluorescence highest in 3D group. Through these observations, it was confirmed that the three-dimensional mesenchymal stem cells were efficiently induced to differentiate into neurons for the same time compared to the two-dimensional mesenchymal stem cells cultured in the conventional way.

Nissl staining results were compared in Fig. 7.4D. First, in the case of the cells observed by the Nissl staining method, phosphorus and Nistle bodies in the nucleus of the cells were stained blue-violet by Cresyl violet reagent. Nistle corpuscle is a characteristic structure observed in nerve cells, and it is a structure containing a lot of ribosomes. The rough endoplasmic reticulum is gathered and observed in a spherical shape.

In the control group, phosphorus-only staining in the nucleus was seen in the cell morphology, and in the 2D ADSCs and ADSCs + GO groups, which were subjected to two-dimensional neural differentiation for 5 days, it was confirmed that the round Nissl bodies were expressed around the nucleus more clearly than in control. . In 3D ADSCs group, cells moved in lumps and formed clusters for one week after they were attached to the floor. It could be confirmed that, unlike 2D ADSCs and ADSCs + GO groups, it was changed to a narrow and elongated shape. This can be seen as evidence that the cell has morphologically differentiated into a nerve cell as it is a form in which the nerve tube is extended during the differentiation process of nerve cells.

In addition, it can be presumed that the three-dimensional implementation of the cell well mimics the actual in vivo environment, thus occupying an advantageous position in differentiation. In addition, it can be seen that the adipose-derived mesenchymal stem cells of the mesenchymal stems are neurons of the ectodermal stems, and that cross-differentiation occurs due to different branches of differentiation. This process is inefficient and difficult in previous studies. In this study, graphene oxide and two factors that realized mesenchymal stem cells in three dimensions worked together to increase the neural differentiation efficiency of mesenchymal stem cells.

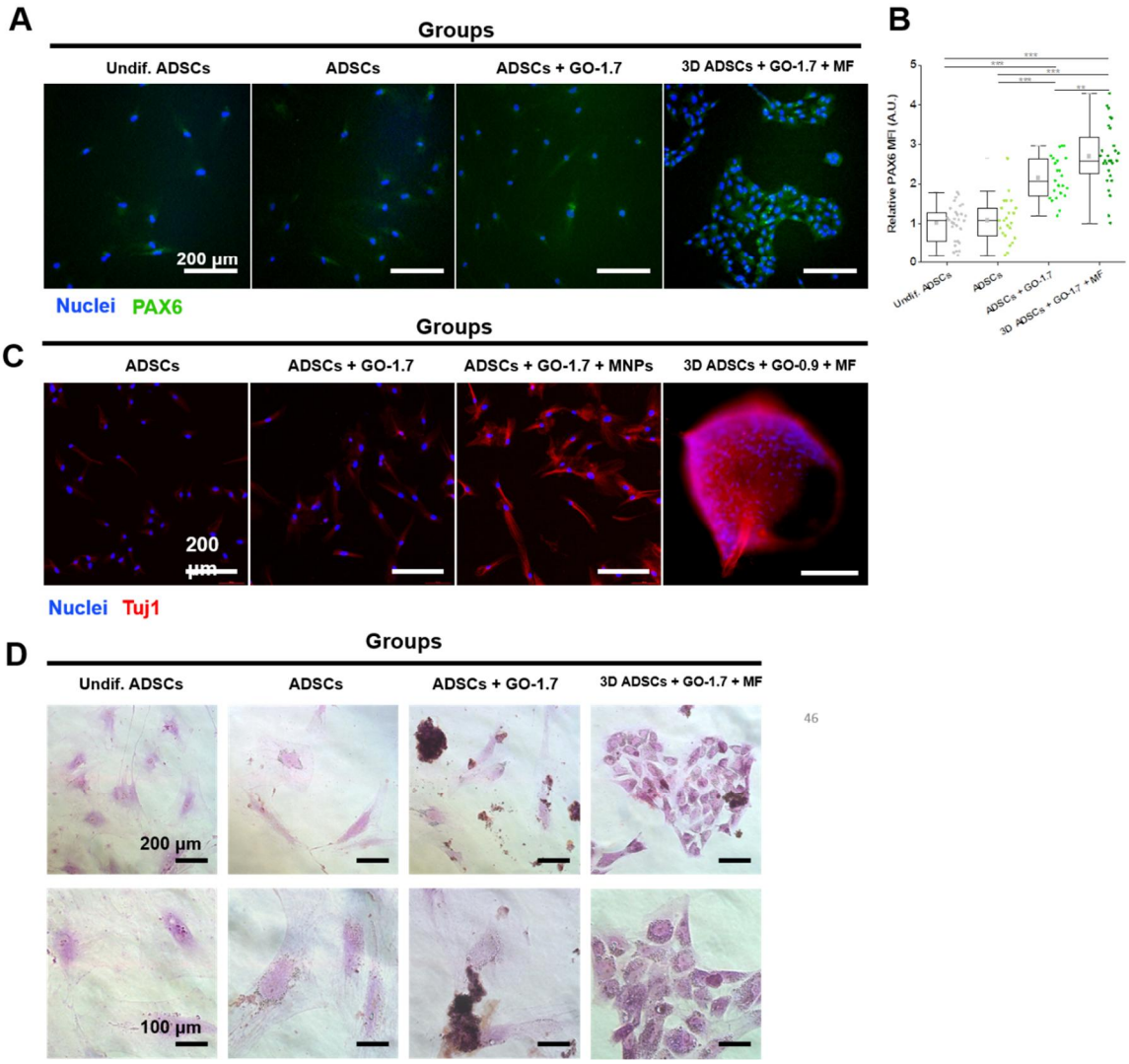

Figure 7.4. Immunocytochemistry of neural induction marker protein and Nissl staining.

(A) Immunocytochemistry of PAX6 protein. (B) Quantification of expression level of PAX6 protein. (C) Immunocytochemistry of Tuj1 protein. (D) Expression of Nissl bodies identified by Nissl staining.

7.5. Conclusions

In this study, mesenchymal stem cells were implemented in three dimensions similar to the in vivo environment using a magnetic force concentration platform using magnetic nanoparticles derived from magnetic bacteria and a tack. and their differentiation efficiency were compared and observed. As a result, it was confirmed that the neural differentiation tendency appeared more clearly in the 3D ADSCs groups, especially in GO-0.9 group.

However, due to the limited research period, the differentiation culture time was short, and there are limitations in the study in that the degree of neuronal differentiation was confirmed only by observation through staining. By extending the incubation period and diversifying the analytical methods, the research can be further developed. In addition, a follow-up study on the mechanism by which neural differentiation is promoted by three-dimensional culture and GO is required.

In conclusion, by forming a three-dimensional cell structure using GO and a magnetic force system, it was possible to increase the neural differentiation efficiency of 3D ADSCs compared to the conventional methods, and similarly to the osteogenic differentiation enhancing effect in a two-dimensional culture situation, neural differentiation was performed by the GO-1.7 experimental group. Also, neural differentiation in 3D culture condition is promoted, and it was confirmed that the GO-0.9 experimental group, which is relatively smaller in size, has the effect of enhancing neuronal differentiation in a three-dimensional culture. Overall, this result suggests that 3D platform using magnetic nanoparticles and graphene oxide sheet would be promising tool for tissue engineering as well as for autologous cell therapy of neurons.

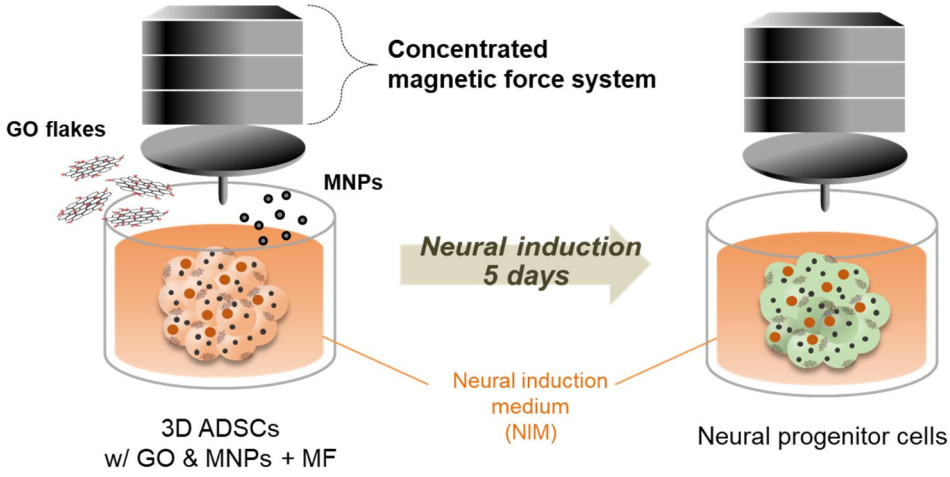

Figure 7.5. Enhanced neural induction of ADSCs spheroid using size-controlled graphene oxide and magnetic nanoparticles.

Chapter 8

Overall discussion and further suggestions

Chapter 8. Overall discussion and further suggestions

In this study, it was possible to promote osteogenic and neural differentiation by introducing size-controlled GO into hMSCs or hESCs through the control of the diameter size of graphene oxide produced in the laboratory, and it was confirmed that these results were obtained by mediating mechanical sensing of stem cells. It was established that the optimal size of graphene oxide flakes depends on the culture environment or cell radius, and that there is a specific size range in diameter of GO flakes that affects the improvement of osteogenic and neural differentiation efficiency or reduction of apoptosis in non-adhesive condition.

The neural differentiation efficiency of the three-dimensional structure incorporating bacterially derived magnetic nanoparticles with the conventional three-dimensional culture method was compared in order to establish that the neural differentiation is promoted by improving the interaction between cells by magnetic force. It was demonstrated that the effects of size-controlled GO flakes on increasing osteogenic differentiation, decreasing apoptosis, and enhancing neural development varies depending on whether hMSCs or hESCs, 2D or 3D culture conditions, and the ideal size of GO.

The largest GO size that could be produced possibly was utilized by narrowing the size distribution by the ball-mill approach. For GO-1.7, the ball-milling duration was 30 min. If the ball-milling time is decreased below that, the ineffectiveness of the size modification was verified. According to earlier studies in our laboratory, the standard ball-milling procedure takes more than an hour. Additionally, compared to other size fractionation techniques in use, ball-milling is a more simple and effective way to manage size distribution of GO flakes.

However, due to the limited research period, the differentiation culture time was short, and there are limitations in the study in that the degree of neural differentiation was confirmed only by observation through neural markers. By extending the incubation period and diversifying the analytical methods, the research can be further developed to identify underlying mechanism of

enhanced neural differentiation. In addition, a follow-up study on the mechanism of GO-cell interaction and enhanced differentiation is promoted by three-dimensional culture and GO is required.

By utilizing biocompatible nanomaterials in practice, these studies can ultimately contribute to the advancement of stem cell treatment and tissue engineering research.

Appendix. Enhanced neural differentiation of 3D human embryonic stem cells *via* magnetic nanoparticle-based physical stimuli

Appendix. Enhanced neural differentiation of 3D human embryonic stem cells *via* magnetic nanoparticle-based physical stimuli

A.1. Introduction

Human embryonic stem cells (hESCs) have been a prospective candidate in regenerative medicine and tissue engineering due to their pluripotency [34, 93]. However, there have been limitations in clinical applications of the hESCs due to side effects such as tumor formation as a result of non-specific differentiation [94, 95]. To take full advantage of the hESCs, a strategy for precisely regulated differentiation of hESCs into targeted cell types has been required [3]. To improve the accuracy for lineage specification, various chemical cues have been used to differentiate hESCs, inducing designated signaling pathways [96-99]. Recently, in addition to such chemical factors, physical environment has been also considered a new key to control the hESC fate [5, 100, 101]. Therefore, generation of human embryoid bodies (hEBs), the 3D organization of hESCs, is suggested as a promising method to regulate the hESCs differentiation [102-104]. Since the hEBs are produced to mimic the biological niche during embryonic development, hESCs in the form of hEBs spontaneously lose self-renewal and differentiate [105, 106].

In our previous studies, we developed high throughput hEB generation and size control system, resulting in production of different size of hEBs: large hEBs with 600 μm on diameter, and small hEBs with 150 μm in diameter [36]. Through the hEB generation method, uniformly sized hEBs were efficiently fabricated without Rho-associated protein kinase (ROCK) inhibitor. And then the effect of hEB size on differentiation into specific germlines was detected. I suggested the proper size for each germinal layer: 150 μm for ectoderm, and 600 μm for endoderm and mesoderm. According to the results, the significance of hEB size on directing the hESC lineage determination was revealed.

For size-controlled hEB generation, magnetic nanoparticles (MNPs) were used, which were isolated from the magnetic bacterium, *Magnetospirillum* sp. AMB-1, and the MNPs exhibited high intracellular delivery efficiency [30, 35, 36, 61, 62]. Magnetic bacteria were cultured under anaerobic conditions and MNPs were synthesized within the bacterial cytoplasm [31, 35]. Since the MNPs possess lipid bilayer of the host bacteria, the particles were readily endocytosed by mammalian cells including stem cells, resulting in magnetization of the cells. Therefore, the MNPs were considered to be a useful tool for simultaneous mechanical stimulation across various forces such as static magnetic field and magnet-derived shear stress [62]. Those magnetic-force-induced biophysical stimulations were applied to enhance tissue-specific differentiation of stem cells [36, 107].

In this study, uniformly sized MNP-hEBs (150 μm in diameter) were generated using concentrated magnetic force and the MNPs, and then neurally differentiated in neural induction medium (NIM) (**Fig. A1**). In order to investigate the improvement of hESC neural inductivity in the form of MNP-hEBs, experimental groups were compared based on addition of 3 variables for neural differentiation: NIM, MNPs, and 3D. Since the hEBs mimic the stiffness of the native tissue [108, 109], uniformly sized hEB generation is considered to be a worthwhile strategy to facilitate neuronal differentiation, providing a similar physical environment to brain tissue. In addition, MNP-hEB production could be an efficient approach enhancing cell-to-cell interactions through magnetic force, resulting in improve neural induction.

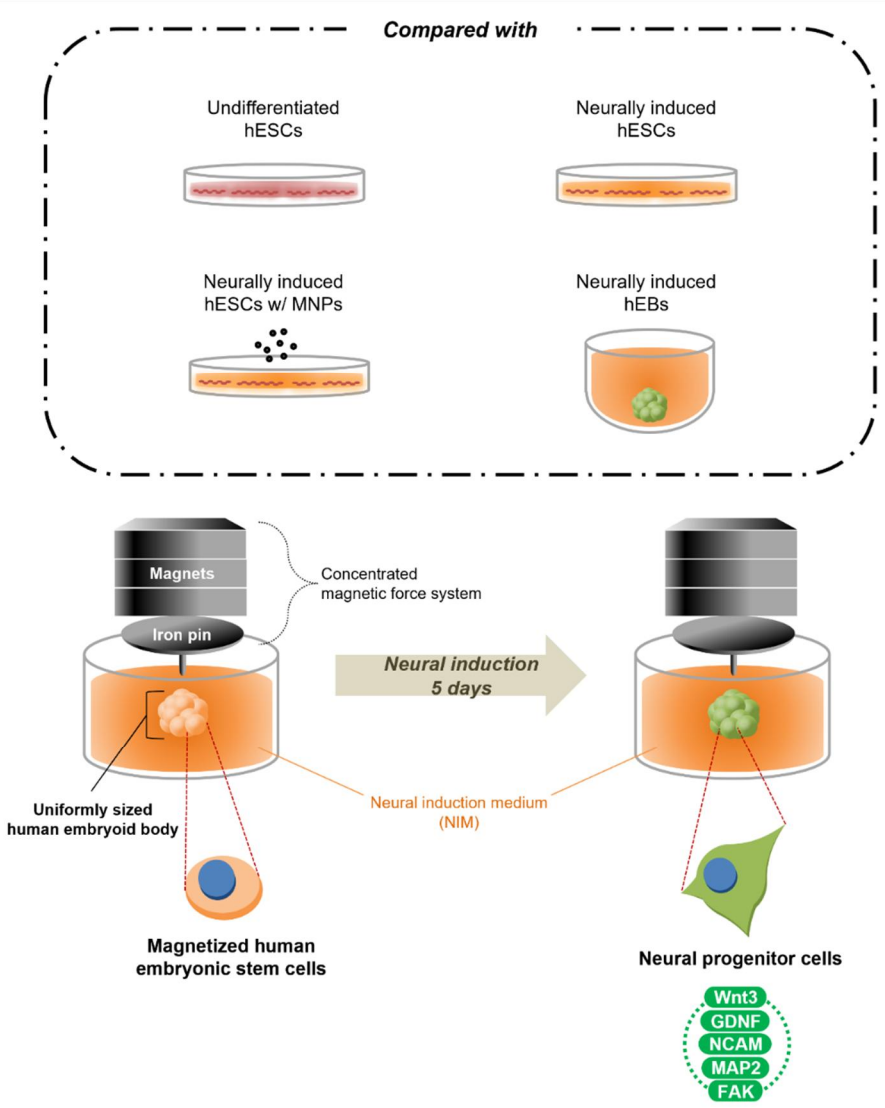

Figure A1. Illustrations for neural induction of 2D and 3D hESCs. MNP-incorporated hEBs were neurally differentiated, and the improvement of neural inductivity was compared with other groups.

A.2. Improved neural induction of MNP-incorporated hEBs, manufactured through a concentrated magnetic force system

In this study, neural inductivity of the hESCs was investigated depending upon variables of 3 factors: NIM, MNPs, and 3D culture condition. For the initial neural differentiation of 2D and 3D hESCs, the hESCs were cultured in NIM instead of hESC culture medium for 5 days, except for the control group (undifferentiated hESCs). Then the MNPs were used for enhanced neural induction, providing 3D organization of the hESCs. Therefore, after isolation from disrupted magnetic bacteria, the MNPs were applied to hESCs and sufficiently magnetized hESCs were separated using static magnets (**Fig. A2A**). In order to generate MNP-hEBs, the MNP-incorporated hESCs were added to concentrated magnetic force system, in which magnetic force of the magnets on the lid was focused at the pinpoint of iron pin under the lid (**Fig. A2B**) [35]. Thus, those magnetized hESCs were gathered at the point of concentrated magnetic force, resulting in generation of 3D hESCs under the surface. Furthermore, the diameter of the generated hEBs was uniformly regulated by adjusting the number of hESCs applied to a well. Therefore, using the MNP-based hEB generation method, uniform hEBs (150 μm in diameter) were manufactured readily, and neural inductivity of MNP-hEBs (hEBs + NIM + MNPs) was investigated comparing with other experimental groups as follows: undifferentiated hESCs as control group (hESCs), conventionally differentiated hESCs with NIM (hESCs + NIM), neurally induced hESCs with NIM and MNPs (hESCs + NIM + MNPs), and conventionally obtained and differentiated hEBs in NIM (hEBs + NIM) (**Fig. A2C and D**).

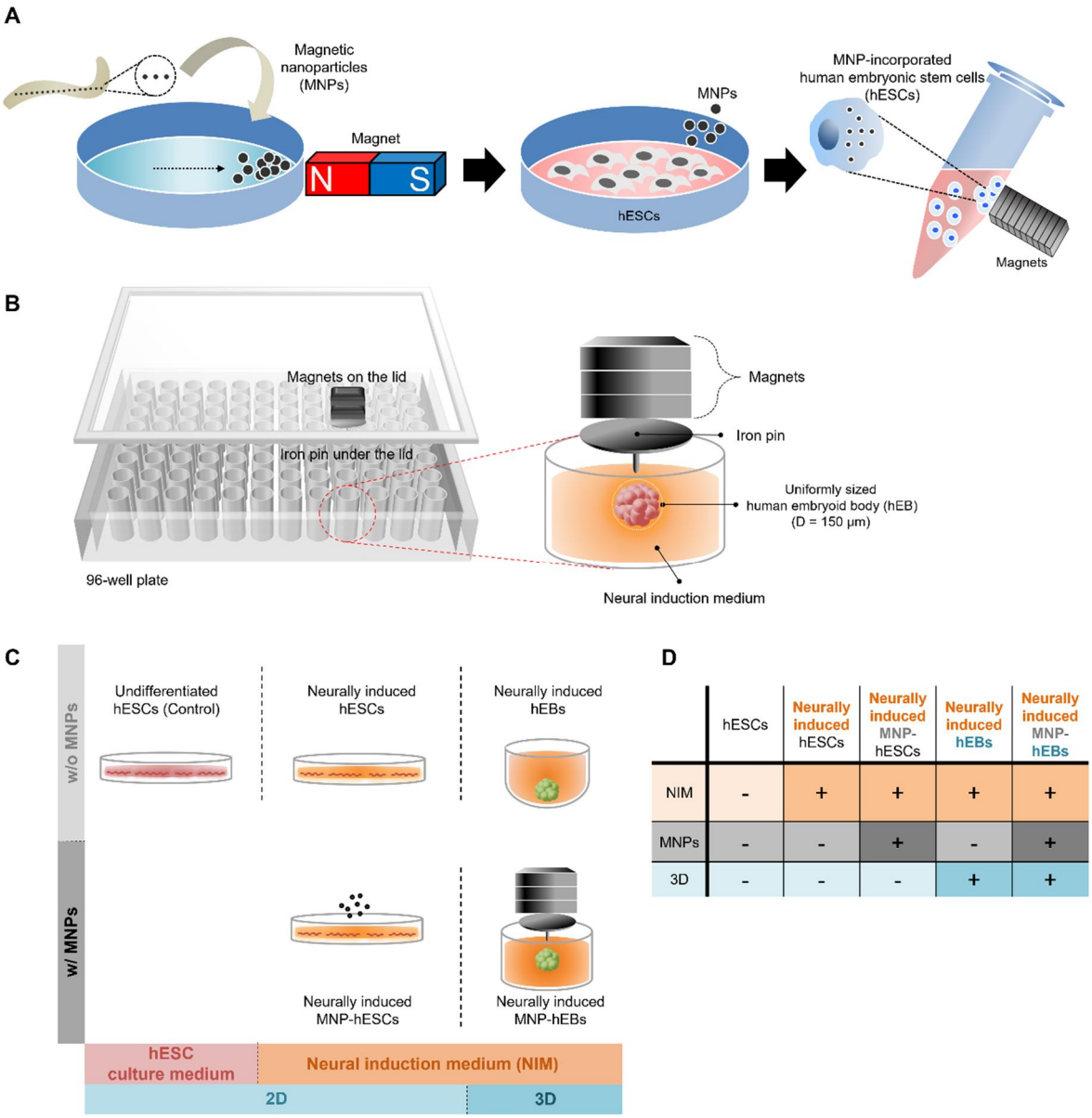

Figure A2. Schematics of MNP-based hEB generation method and designation of experimental groups. (A) Overall steps of hESC magnetization. After ultrasonic disruption of magnetic bacteria, MNPs were isolated with neodymium magnets. The hESCs were treated with collected MNPs and MNP-incorporated hESCs were separated using magnets. (B) Schematics for concentrated magnetic force system and neural induction of hEBs. To efficiently differentiate the hESCs into neural commitments, a high throughput method utilizing the MNPs and concentrated magnetic force system in a 96-well plate was applied. Therefore, uniformly sized hEBs (150 μm in

diameter) were produced. (C) Illustrations of experimental groups: Undifferentiated pluripotent hESCs as the control group (hESCs); Neurally differentiated hESCs (hESCs + NIM); Neurally induced hESCs with MNPs (hESCs + NIM + MNPs); Neurally induced hEBs, generated in the non-coated round bottom plates (hEBs + NIM); Neurally induced MNP-incorporated hEBs (hEBs + NIM + MNPs). (D) Each experimental group was decided by the existence of three factors. Firstly, NIM instead of hESC culture medium. Secondly, MNPs. And lastly, 3D cultivation environment.

A.3. Morphological analysis of neurally induced hESCs

Shape of the hESCs was observed to validate neural differentiation (**Fig. A3A**). In the control group (hESCs), typical morphology of pluripotent hESCs was observed. The cells presented a round-shaped appearance, in compact colonies formed by the intact hESCs. Otherwise, in neurally induced hESCs (hESCs + NIM), not only round cells but also angular cells co-existed. And those angular cells were observed where the cell density was low, far from the center of colonies. In neurally induced MNP-hESCs (hESCs + NIM + MNPs), neurally induced hEBs (hEBs + NIM), and neurally induced MNP-hEBs (hEBs + NIM + MNPs), a larger number of angular cells were observed, and prominent neurite protrusions were shown. Several neurites sprouted from one cell, and some of those neurites were significantly longer.

To quantify the cell morphology related to neural induction, number of neurites per cell was examined (**Figs. A3B and C**). In the control group (hESCs), cells remained spherical, resulting in the absence of neurite-extending cells, whereas all the other groups (neurally induced 2D and 3D hESCs) expressed angular-shaped cells with neurites. The ratio of cells without neurites significantly decreased, while the proportion of cells with neurites increased according to neural induction with 3 variables (NIM, MNPs, and 3D). In particular, not only the ratio of cells with more than one neurite, but also the average number of neurites per cell has been remarkably increased in neurally induced MNP-hEBs (hEBs + NIM + MNPs).

Also, the length of neurites was calculated as follows: length of primary neurites (the longest neurite in a cell), summarized length of primary and secondary neurites (the longest neurite + the second longest neurite in a cell), and summarized length of total neurites from each cell (**Figs. A3D and E**). As a result, the length of primary neurites (red line in **Fig. A3D**) and summarized length of primary and secondary neurites (green line in **Fig. A3D**) significantly increased in MNP-treated groups (hESCs + NIM + MNPs, and hEBs + NIM + MNPs) compared with the conventionally differentiated hESCs (hESCs + NIM) ($p < 0.001$, respectively). Regarding the length of total neurites from one cell, the value remarkably increased in neurally induced MNP-hESCs (hESCs +

NIM + MNPs) and both types of hEBs (hEBs + NIM, and hEBs + NIM + MNPs), compared to neurally induced hESCs (hESCs + NIM) (blue line in **Fig. A3D**, $p < 0.001$).

A

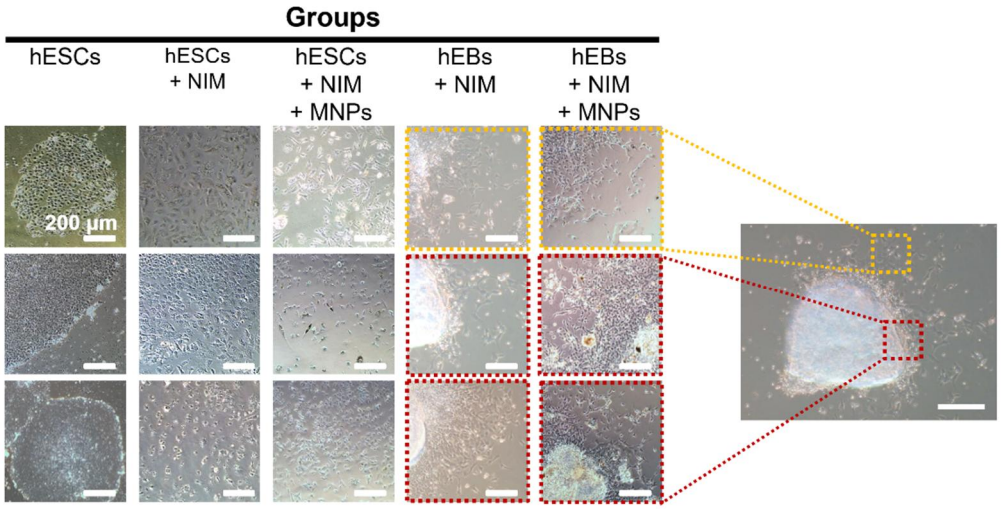

B

Proportion of cells (%)

Number of neurites	hESCs	hESCs + NIM	hESCs + NIM + MNPs	hEBs + NIM	hEBs + NIM + MNPs
0	100	64.1	9.6	43.4	10.5
1	0	18.9	33.8	32.1	14.3
2	0	6.8	25.0	18.9	30.3
≥ 3	0	10.2	31.6	5.7	44.7

C

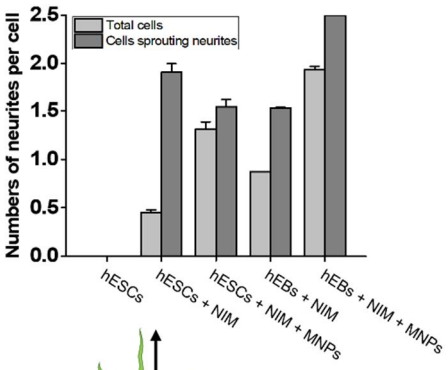

D

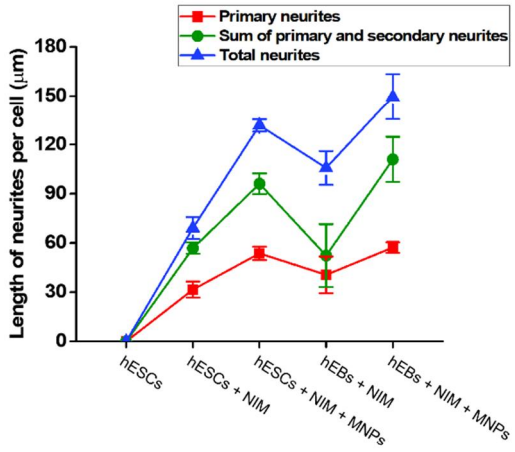

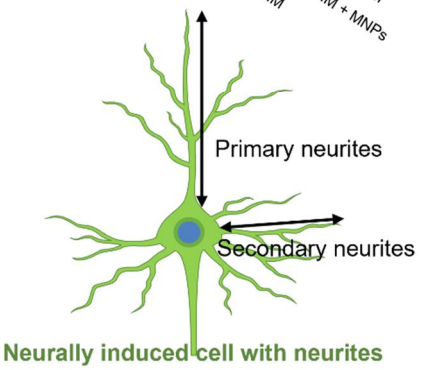

E

Neurites	Length of neurites per cell (μm) Mean ± SD			
	hESCs +NIM	hESCs + NIM + MNPs	hEBs + NIM	hEBs + NIM + MNPs
Primary	31.57±4.90	53.68±4.05	40.59±11.18	57.27±3.24
Primary + secondary	56.81±3.46	96.12±6.29	52.29±19.17	111.00±13.78
Total	69.14±6.70	131.76±3.79	105.77±10.34	149.51±13.88

Figure A3. Morphological analysis of neurally induced 2D and 3D hESCs. (A) Microscopic images of hESCs in experimental groups. Yellow dotted squares indicate migrated cells from the 3D aggregates. Red dotted squares indicate the edge of hEBs, including 3D aggregates and migrated cells. (B), (C) Number of neurites per cell. (B) The proportion of cells (%) according to the number of neurites in all experimental groups. (C) The number of neurites in total cells, including the cells without neurites, was demonstrated as black bars, and the number of neurites in only cells sprouting neurites, was represented as gray bars. (D), (E) Length of neurites per cell. (D) The length of primary neurites (red line), the sum of primary and secondary neurites (green line), and sum of total neurites (blue line) were investigated, respectively. (E) Mean values of neurite length. Scale bars, 200 μm.

A.4. Genetical analysis of neural induction marker genes

To investigate neural induction, genetical analysis was performed, measuring mRNA expression levels (**Fig. A3**). According to **Fig. A3A**, the expression of *OCT4*, a pluripotency marker [33], statistically decreased in neurally induced 2D and 3D hESCs, compared with the value of control group (hESCs, horizontal line indicating 1).

In **Fig. A4B**, expression of *GAP43* was compared, and thus neuronal growth and neurite formation was investigated [110]. Statistically significant increase was observed depending upon addition of variables for neural induction (NIM, MNPs, and 3D). Therefore, relative fold induction values remarkably increased in neurally induced hESCs (hESCs + NIM) comparing with the control (hESCs), also in neurally induced MNP-hESCs (hESCs + NIM + MNPs) than the neurally induced hESCs (hESCs + NIM), finally in neurally induced MNP-hEBs (hEBs + NIM + MNPs) than neurally induced MNP-hESCs (hESCs + NIM + MNPs) ($p < 0.001$).

Expression of *TUBB3* was compared in **Fig. A4C**, which indicates microtubule formation of early committed neurons [111]. The relative value was upregulated in neurally induced hESCs (hESCs + NIM) and MNP-hESCs (hESCs + NIM + MNPs), compared with not only the control (hESCs), but also neurally induced hEBs (hEBs + NIM) and MNP-hEBs (hEBs + NIM + MNPs). Therefore, neurally induced 2D hESCs in attached condition showed enhanced expression of *TUBB3* compared with 3D hESCs in suspended condition.

Regarding *NES*, a specific marker of neural stem cells related to the growth of intermediate filament and axon of neural-precursor cells, the expression level significantly increased in neurally induced MNP-hESCs (hESCs + NIM + MNPs), and neurally induced hEBs regardless of MNP existence (hEBs + NIM, and hEBs + NIM + MNPs), compared with the control (hESCs) and neurally induced hESCs (hESCs + NIM) ($p < 0.001$, respectively) (**Fig. A4D**).

Similar tendency was observed in expression of *GFAP*, an astrocyte marker indicating intermediate filament growth and cell morphology maintenance (**Fig. A4E**). Expression of *GFAP*

mostly increased in neurally induced MNP-hEBs (hEBs + NIM + MNPs), comparing to the other experimental groups.

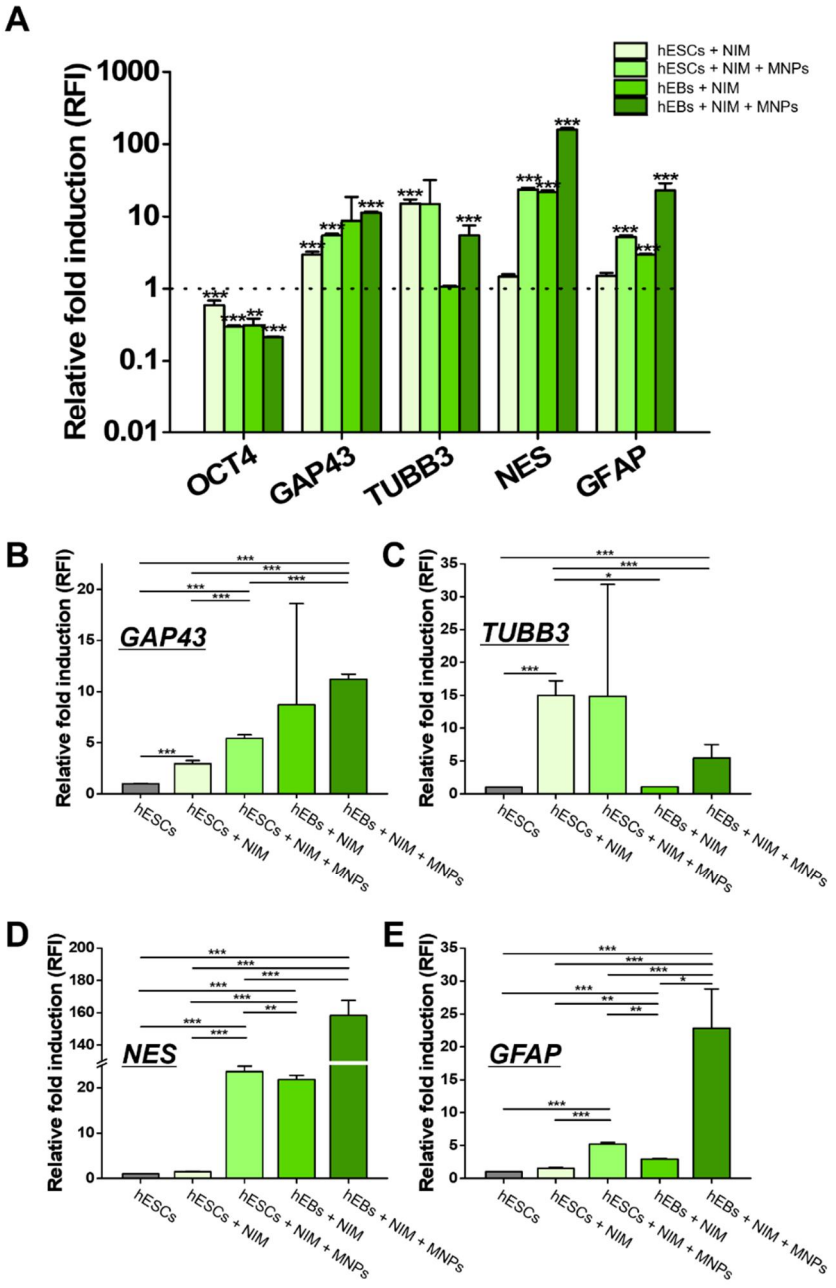

Figure A4. Genetical analysis of a pluripotency marker gene and neural induction marker genes. (A) Relative expression of mRNA in all the experimental groups. The values of each gene were normalized by the expression level in control (hESCs). Expression of *GAP43* (B), *TUBB3* (C), *NES* (D), and *GFAP* (E) was compared among the groups. *P < 0.05, **P < 0.01, and ***P < 0.001.

A.5. Related mechanisms to accelerated neural induction of hEBs

To verify the related mechanisms of activated neural induction of in MNP-hEBs (hEBs + NIM + MNPs), possible signal pathways which may have been involved were suggested and investigated. Therefore, the expression of related signaling proteins was examined with western blot. The proteins investigated for the analysis were as follows: GDNF, representing the dopaminergic neuronal pathways; NCAM, indicating cell adhesions and intercellular communications; MAP2, related to microtubule growth and neural development promoted through mechanotransduction; FAK, representing the induced mechanical stimuli [112-114].

The expression of Wnt3 and Wnt5α protein was investigated through western blot with immunocytochemically examined signaling proteins (**Fig. A5A, B**). As a result, expressed Wnt3 was remarkably observed in neurally induced MNP-hEBs (hEBs + NIM + MNPs), and Wnt5α was expressed in neurally induced hESCs (hESCs + NIM). Also the result showed that GDNF, MAP2, and FAK were similarly expressed in both groups, while the expression of NCAM showed enhancement in neurally induced MNP-hEBs (hEBs + NIM + MNPs), compared to the neurally induced hESCs (hESCs + NIM). Therefore, neural induction-related signaling proteins were observed in neurally induced MNP-hEBs (hEBs + NIM + MNPs), in which physical stimulation was activated as much as in conventionally differentiated hESCs (hESCs + NIM), the adherent cells.

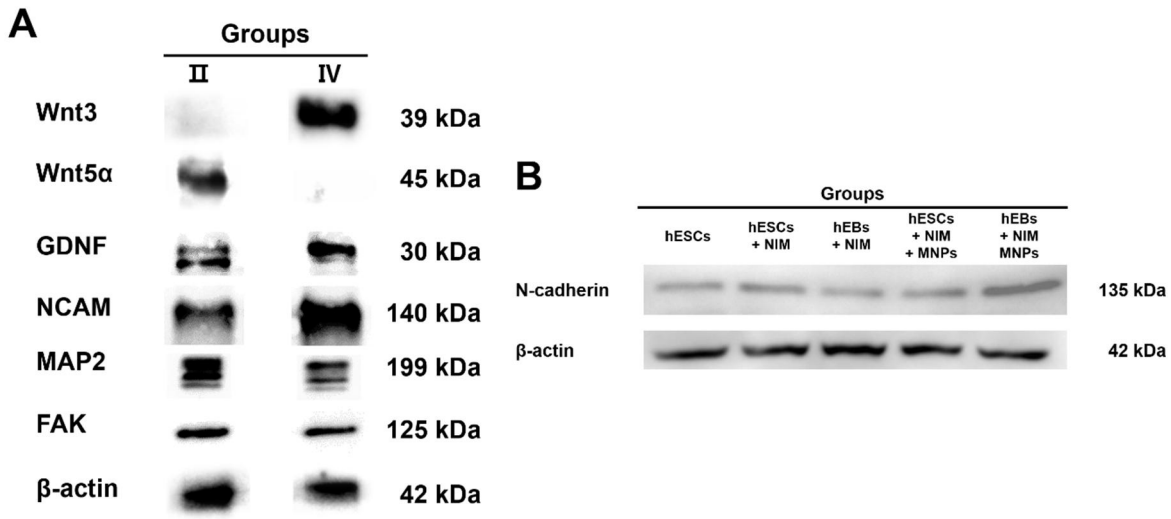

Figure A5. Analysis of signaling pathways of the neurally induced 2D and 3D hESCs. (A) Western blotting of proteins related to cell signaling pathway and cell-to-cell interactions. As a reference protein, β-actin was utilized. Wnt3 was expressed only in neurally induced MNP-hEBs (hEBs + NIM + MNPs), while Wnt5α was expressed only in neurally induced hESCs (hESCs + NIM). (B) Western blotting of N-cadherin protein for assessment of cell-to-cell interactin.

A.6. Conclusions

Although there have been many efforts to regenerate the nerve tissue by differentiating the pluripotent stem cells into neuronal cells, the neural lineage specification requires long-term cultivation and laborious steps. In this study, MNP-incorporated and uniformly sized hEBs were generated for improved neural differentiation. The neural inductivity was compared in neurally induced MNP-hEBs (hEBs + NIM + MNPs) with the other experimental groups in order to define the effect of each variable for neural differentiation (NIM, MNPs, and 3D): control (hESCs); conventionally differentiated hESCs (hESCs + NIM); neurally induced MNP-hESCs (hESCs + NIM + MNPs); neurally induced hEBs (hEBs + NIM). According to the results, MNP-hEBs showed improved initial neural differentiation in morphological analysis, genetical investigation, immunocytochemistry and western blotting. Furthermore, neurally induced MNP-hEBs followed Wnt3 signaling pathway and possessed dopamine affinity and enhanced cell-to-cell interactions. Therefore, MNP-based hEB size control method proposed in this study would be a useful tool for enhanced neuronal differentiation and nerve tissue regeneration. In addition, this technique could be applied to accelerate initial lineage-specific differentiation of hESCs, directing cellular commitments with simulation of embryogenesis.

Bibliography

[1] M.F. Pera, A.O. Trounson, Human embryonic stem cells: prospects for development, Development 131(22) (2004) 5515-25.

[2] W. Zakrzewski, M. Dobrzynski, M. Szymonowicz, Z. Rybak, Stem cells: past, present, and future, Stem Cell. Res. Ther. 10(1) (2019) 68.

[3] Y.J. Ren, H. Zhang, H. Huang, X.M. Wang, Z.Y. Zhou, F.Z. Cui, Y.H. An, In vitro behavior of neural stem cells in response to different chemical functional groups, Biomaterials 30(6) (2009) 1036-44.

[4] A.J. Engler, S. Sen, H.L. Sweeney, D.E. Discher, Matrix elasticity directs stem cell lineage specification, Cell 126(4) (2006) 677-89.

[5] F. Guilak, D.M. Cohen, B.T. Estes, J.M. Gimble, W. Liedtke, C.S. Chen, Control of stem cell fate by physical interactions with the extracellular matrix, Cell Stem Cell 5(1) (2009) 17-26.

[6] J.K. Ivins, P.D. Yurchenco, A.D. Lander, Regulation of neurite outgrowth by integrin activation, J. Neurosci. 20(17) (2000) 6551-60.

[7] A. Halim, Q. Luo, Y. Ju, G. Song, A Mini Review Focused on the Recent Applications of Graphene Oxide in Stem Cell Growth and Differentiation, Nanomaterials (Basel) 8(9) (2018).

[8] K. Krukiewicz, D. Putzer, N. Stuendl, B. Lohberger, F. Awaja, Enhanced Osteogenic Differentiation of Human Primary Mesenchymal Stem and Progenitor Cultures on Graphene Oxide/Poly(methyl methacrylate) Composite Scaffolds, Materials 13(13) (2020) 2991.

[9] M. Kalbacova, A. Broz, J. Kong, M. Kalbac, Graphene substrates promote adherence of human osteoblasts and mesenchymal stromal cells, Carbon 48(15) (2010) 4323-4329.

[10] K.Y. Shin, S. Lee, S. Hong, J. Jang, Graphene size control via a mechanochemical method and electroresponsive properties, ACS Appl Mater Interfaces 6(8) (2014) 5531-7.

[11] Z. Guo, C. Sun, H. Yang, H. Gao, N. Liang, J. Wang, S. Hu, N. Ren, J. Pang, J. Wang, N. Meng, L. Han, H. Liu, Regulation of Neural Differentiation of ADMSCs using Graphene-Mediated Wireless-Localized Electrical Signals Driven by Electromagnetic Induction, Adv Sci (Weinh) 9(14) (2022) e2104424.

[12] S. Reddy, L.M. He, S. Ramakrishana, H.R. Luo, Graphene nanomaterials for regulating stem cell fate in neurogenesis and their biocompatibility, Current Opinion in Biomedical Engineering 10 (2019) 69-78.

[13] O. Akhavan, E. Ghaderi, E. Abouei, S. Hatamie, E. Ghasemi, Accelerated differentiation of neural stem cells into neurons on ginseng-reduced graphene oxide sheets, Carbon 66 (2014) 395-406.

[14] Z. Du, C. Wang, R. Zhang, X. Wang, X. Li, Applications of Graphene and Its Derivatives in Bone Repair: Advantages for Promoting Bone Formation and Providing Real-Time Detection, Challenges and Future Prospects, Int J Nanomedicine 15 (2020) 7523-7551.

[15] J. Heo, J. Choi, J.Y. Kim, H. Jeong, D. Choi, U. Han, J.H. Park, H.H. Park, J. Hong, 2D graphene oxide particles induce unwanted loss in pluripotency and trigger early differentiation in human pluripotent stem cells, J Hazard Mater 414 (2021) 125472.

[16] J. de Boer, R. Siddappa, C. Gaspar, A. van Apeldoorn, R. Fodde, C. van Blitterswijk, Wnt signaling inhibits osteogenic differentiation of human mesenchymal stem cells, Bone 34(5) (2004) 818-26.

[17] S. Even-Ram, V. Artym, K.M. Yamada, Matrix control of stem cell fate, Cell 126(4) (2006) 645-7.

[18] M.Z. Ozair, C. Kintner, A.H. Brivanlou, Neural induction and early patterning in vertebrates, Wiley Interdiscip Rev Dev Biol 2(4) (2013) 479-98.

[19] B.E. Reubinoff, M.F. Pera, C.Y. Fong, A. Trounson, A. Bongso, Embryonic stem cell lines from human blastocysts: somatic differentiation in vitro, Nat Biotechnol 18(4) (2000) 399-404.

[20] A.O. Trounson, The derivation and potential use of human embryonic stem cells, Reprod Fertil Dev 13(7-8) (2001) 523-32.

[21] F.H. Gage, Mammalian neural stem cells, Science 287(5457) (2000) 1433-8.

[22] E. Garcia-Alegria, M. Iluit, M. Stefanska, C. Silva, S. Heeg, S.J. Kimber, V. Kouskoff, G. Lacaud, A. Vijayaraghavan, K. Batta, Graphene Oxide promotes embryonic stem cell differentiation to haematopoietic lineage, Scientific Reports 6 (2016) 1-13.

[23] O. Akhavan, E. Ghaderi, The use of graphene in the self-organized differentiation of human neural stem cells into neurons under pulsed laser stimulation, J Mater Chem B 2(34) (2014) 5602-5611.

[24] C.H. Kim, T.H. Kim, Graphene Hybrid Materials for Controlling Cellular Microenvironments, Materials 13(18) (2020) 4008.

[25] J. Jagiello, M. Sekula-Stryjewska, S. Noga, E. Adamczyk, M. Dzwigonska, M. Kurcz, K. Kurp, M. Winkowska-Struzik, E. Karnas, D. Boruczkowski, Z. Madeja, L. Lipinska, E.K. Zuba-Surma, Impact of Graphene-Based Surfaces on the Basic Biological Properties of Human Umbilical Cord Mesenchymal Stem Cells: Implications for Ex Vivo Cell Expansion Aimed at Tissue Repair, International Journal of Molecular Sciences 20(18) (2019) 4561.

[26] W. Guo, J. Qiu, J. Liu, H. Liu, Graphene microfiber as a scaffold for regulation of neural stem cells differentiation, Sci Rep 7(1) (2017) 5678.

[27] N. Shadjou, M. Hasanzadeh, Graphene and its nanostructure derivatives for use in bone tissue engineering: Recent advances, J Biomed Mater Res A 104(5) (2016) 1250-75.

[28] P.R.Y. Gangavarapu, P.C. Lokesh, K.N. Bhat, A.K. Naik, Graphene Electrodes as Barrier-Free Contacts for Carbon Nanotube Field-Effect Transistors, Ieee Transactions on Electron Devices 64(10) (2017) 4335-4339.

[29] S. Lee, J.Y. Hong, J. Jang, Multifunctional graphene sheets embedded in silicone encapsulant for superior performance of light-emitting diodes, ACS Nano 7(7) (2013) 5784-90.

[30] J.A. Kim, H.J. Lee, H.J. Kang, T.H. Park, The targeting of endothelial progenitor cells to a specific location within a microfluidic channel using magnetic nanoparticles, Biomed Microdevices 11(1) (2009) 287-96.

[31] S. Seong, T.H. Park, Swimming characteristics of magnetic bacterium, Magnetospirillum sp AMB-1, and implications as toxicity measurement, Biotechnology and Bioengineering 76(1) (2001) 11-16.

[32] S. Kim, S.S. Lee, B. Son, J.A. Kim, N.S. Hwang, T.H. Park, Partially Digested Osteoblast Cell Line-Derived Extracellular Matrix Induces Rapid Mineralization and Osteogenesis, ACS Biomater Sci Eng 7(3) (2021) 1134-1146.

[33] H. Lee, S.H.L. Kim, H. Yoon, J. Ryu, H.H. Park, N.S. Hwang, T.H. Park, Intracellular Delivery of Recombinant RUNX2 Facilitated by Cell-Penetrating Protein for the Osteogenic Differentiation of hMSCs, ACS Biomater Sci Eng 6(9) (2020) 5202-5214.

[34] L.A. Boyer, T.I. Lee, M.F. Cole, S.E. Johnstone, S.S. Levine, J.P. Zucker, M.G. Guenther, R.M. Kumar, H.L. Murray, R.G. Jenner, D.K. Gifford, D.A. Melton, R. Jaenisch, R.A. Young, Core transcriptional regulatory circuitry in human embryonic stem cells, Cell 122(6) (2005) 947-56.

[35] J.A. Kim, J.H. Choi, M. Kim, W.J. Rhee, B. Son, H.K. Jung, T.H. Park, High-throughput generation of spheroids using magnetic nanoparticles for three-dimensional cell culture, Biomaterials 34(34) (2013) 8555-63.

[36] B. Son, J.A. Kim, S. Cho, G.J. Jeong, B.S. Kim, N.S. Hwang, T.H. Park, Lineage Specific Differentiation of Magnetic Nanoparticle-Based Size Controlled Human Embryoid Body, ACS Biomater Sci Eng 3(8) (2017) 1719-1729.

[37] H. Lee, Y.H. An, T.K. Kim, J. Ryu, G.K. Park, M.J. Park, J. Ko, H. Kim, H.S. Choi, N.S. Hwang, T.H. Park, Enhancement of Wound Healing Efficacy by Increasing the Stability and Skin-Penetrating Property of bFGF Using 30Kc19alpha-Based Fusion Protein, Adv Biol (Weinh) 5(1) (2021) e2000176.

[38] S. Kim, H. Lee, J.A. Kim, T.H. Park, Prevention of collagen hydrogel contraction using polydopamine-coating and alginate outer shell increases cell contractile force, Biomater Adv 136 (2022) 212780.

[39] T. Szabo, P. Maroni, I. Szilagyi, Size-dependent aggregation of graphene oxide, Carbon 160 (2020) 145-155.

[40] Y.Y. Khine, X.J. Ren, D.W. Chu, Y. Nishina, T. Foller, R. Joshi, Surface Functionalities of Graphene Oxide with Varying Flake Size, Industrial & Engineering Chemistry Research 61(19) (2022) 6531-6536.

[41] X.N. Chen, X.H. Wang, D. Fang, A review on C1s XPS-spectra for some kinds of carbon materials, Fullerenes Nanotubes and Carbon Nanostructures 28(12) (2020) 1048-1058.

[42] D. Yang, A. Velamakanni, G. Bozoklu, S. Park, M. Stoller, R.D. Piner, S. Stankovich, I. Jung, D.A. Field, C.A. Ventrice, R.S. Ruoff, Chemical analysis of graphene oxide films after heat

and chemical treatments by X-ray photoelectron and Micro-Raman spectroscopy, Carbon 47(1) (2009) 145-152.

[43] S.S. Nanda, D.K. Yi, K. Kim, Study of antibacterial mechanism of graphene oxide using Raman spectroscopy, Sci Rep 6(1) (2016) 28443.

[44] S. Stankovich, R.D. Piner, S.T. Nguyen, R.S. Ruoff, Synthesis and exfoliation of isocyanate-treated graphene oxide nanoplatelets, Carbon 44(15) (2006) 3342-3347.

[45] C. Sun, Devin L. Wakefield, Y. Han, David A. Muller, David A. Holowka, Barbara A. Baird, William R. Dichtel, Graphene Oxide Nanosheets Stimulate Ruffling and Shedding of Mammalian Cell Plasma Membranes, Chem 1(2) (2016) 273-286.

[46] H. Zhang, C. Peng, J. Yang, M. Lv, R. Liu, D. He, C. Fan, Q. Huang, Uniform ultrasmall graphene oxide nanosheets with low cytotoxicity and high cellular uptake, ACS Appl Mater Interfaces 5(5) (2013) 1761-7.

[47] T. Lammel, P. Boisseaux, M.L. Fernandez-Cruz, J.M. Navas, Internalization and cytotoxicity of graphene oxide and carboxyl graphene nanoplatelets in the human hepatocellular carcinoma cell line Hep G2, Part. Fibre Toxicol. 10(1) (2013) 27.

[48] O. Akhavan, E. Ghaderi, A. Akhavan, Size-dependent genotoxicity of graphene nanoplatelets in human stem cells, Biomaterials 33(32) (2012) 8017-25.

[49] Z. Chen, C. Yu, I.A. Khan, Y. Tang, S. Liu, M. Yang, Toxic effects of different-sized graphene oxide particles on zebrafish embryonic development, Ecotoxicol Environ Saf 197 (2020) 110608.

[50] L. Lin, X. Zhuang, R. Huang, S. Song, Z. Wang, S. Wang, L. Cheng, R. Zhu, Size-Dependent Effects of Suspended Graphene Oxide Nanoparticles on the Cellular Fate of Mouse Neural Stem Cells, Int J Nanomedicine 15 (2020) 1421-1435.

[51] Q. Mu, G. Su, L. Li, B.O. Gilbertson, L.H. Yu, Q. Zhang, Y.P. Sun, B. Yan, Size-dependent cell uptake of protein-coated graphene oxide nanosheets, ACS Appl Mater Interfaces 4(4) (2012) 2259-66.

[52] S. Gurunathan, M.-H. Kang, M. Jeyaraj, J.-H. Kim, Differential Cytotoxicity of Different Sizes of Graphene Oxide Nanoparticles in Leydig (TM3) and Sertoli (TM4) Cells, Nanomaterials 9(2) (2019) 139.

[53] E.S. Kang, I. Song, D.S. Kim, U. Lee, J.K. Kim, H. Son, J. Min, T.H. Kim, Size-dependent effects of graphene oxide on the osteogenesis of human adipose-derived mesenchymal stem cells, Colloids Surf B Biointerfaces 169 (2018) 20-29.

[54] T.J. Lee, S. Park, S.H. Bhang, J.K. Yoon, I. Jo, G.J. Jeong, B.H. Hong, B.S. Kim, Graphene enhances the cardiomyogenic differentiation of human embryonic stem cells, Biochem Biophys Res Commun 452(1) (2014) 174-80.

[55] G. Jing, Z. Wang, X. Zhuang, X. He, H. Wu, Q. Wang, L. Cheng, Z. Liu, S. Wang, R. Zhu, Suspended graphene oxide nanosheets maintain the self-renewal of mouse embryonic stem cells via down-regulating the expression of Vinculin, Biomaterials 171 (2018) 1-11.

[56] H. Xie, T. Cao, A. Franco-Obregón, V. Rosa, Graphene-Induced Osteogenic Differentiation Is Mediated by the Integrin/FAK Axis, International Journal of Molecular Sciences 20(3) (2019) 574.

[57] D.E. Jaalouk, J. Lammerding, Mechanotransduction gone awry, Nat Rev Mol Cell Biol 10(1) (2009) 63-73.

[58] J. Zonderland, L. Moroni, Steering cell behavior through mechanobiology in 3D: A regenerative medicine perspective, Biomaterials 268 (2021) 120572.

[59] C. Wei, Z. Liu, F. Jiang, B. Zeng, M. Huang, D. Yu, Cellular behaviours of bone marrow-derived mesenchymal stem cells towards pristine graphene oxide nanosheets, Cell proliferation 50(5) (2017) e12367.

[60] P. Hersen, B. Ladoux, Biophysics: Push it, pull it, Nature 470(7334) (2011) 340-1.

[61] S. Cho, M.J. Shon, B. Son, G.S. Eun, T.Y. Yoon, T.H. Park, Tension exerted on cells by magnetic nanoparticles regulates differentiation of human mesenchymal stem cells, Biomater Adv 139 (2022) 213028.

[62] B. Son, H.D. Kim, M. Kim, J.A. Kim, J. Lee, H. Shin, N.S. Hwang, T.H. Park, Physical Stimuli-Induced Chondrogenic Differentiation of Mesenchymal Stem Cells Using Magnetic Nanoparticles, Adv Healthc Mater 4(9) (2015) 1339-47.

[63] J.A. Kim, E.Y. Jang, T.J. Kang, S. Yoon, R. Ovalle-Robles, W.J. Rhee, T. Kim, R.H. Baughman, Y.H. Kim, T.H. Park, Regulation of morphogenesis and neural differentiation of

human mesenchymal stem cells using carbon nanotube sheets, Integr. Biol. (Camb.) 4(6) (2012) 587-94.

[64] Q. Chen, P. Shou, L. Zhang, C. Xu, C. Zheng, Y. Han, W. Li, Y. Huang, X. Zhang, C. Shao, A.I. Roberts, A.B. Rabson, G. Ren, Y. Zhang, Y. Wang, D.T. Denhardt, Y. Shi, An osteopontin-integrin interaction plays a critical role in directing adipogenesis and osteogenesis by mesenchymal stem cells, Stem Cells 32(2) (2014) 327-37.

[65] R.M. Salasznyk, W.A. Williams, A. Boskey, A. Batorsky, G.E. Plopper, Adhesion to Vitronectin and Collagen I Promotes Osteogenic Differentiation of Human Mesenchymal Stem Cells, J Biomed Biotechnol 2004(1) (2004) 24-34.

[66] E.A. Cavalcanti-Adam, T. Volberg, A. Micoulet, H. Kessler, B. Geiger, J.P. Spatz, Cell spreading and focal adhesion dynamics are regulated by spacing of integrin ligands, Biophys. J. 92(8) (2007) 2964-74.

[67] N. Huebsch, P.R. Arany, A.S. Mao, D. Shvartsman, O.A. Ali, S.A. Bencherif, J. Rivera-Feliciano, D.J. Mooney, Harnessing traction-mediated manipulation of the cell/matrix interface to control stem-cell fate, Nat Mater 9(6) (2010) 518-26.

[68] B.D. Cosgrove, K.L. Mui, T.P. Driscoll, S.R. Caliari, K.D. Mehta, R.K. Assoian, J.A. Burdick, R.L. Mauck, N-cadherin adhesive interactions modulate matrix mechanosensing and fate commitment of mesenchymal stem cells, Nat Mater 15(12) (2016) 1297-1306.

[69] U. Horzum, B. Ozdil, D. Pesen-Okvur, Step-by-step quantitative analysis of focal adhesions, MethodsX 1 (2014) 56-9.

[70] C.F. Natale, M. Ventre, P.A. Netti, Tuning the material-cytoskeleton crosstalk via nanoconfinement of focal adhesions, Biomaterials 35(9) (2014) 2743-51.

[71] P.S. Mathieu, E.G. Loboa, Cytoskeletal and Focal Adhesion Influences on Mesenchymal Stem Cell Shape, Mechanical Properties, and Differentiation Down Osteogenic, Adipogenic, and Chondrogenic Pathways, Tissue Engineering Part B-Reviews 18(6) (2012) 436-444.

[72] M. Bruderer, R.G. Richards, M. Alini, M.J. Stoddart, Role and regulation of RUNX2 in osteogenesis, Eur Cell Mater 28(28) (2014) 269-86.

[73] Y. Tang, S.J. Weiss, Snail/Slug-YAP/TAZ complexes cooperatively regulate mesenchymal stem cell function and bone formation, Cell Cycle 16(5) (2017) 399-405.

[74] C.B. Khatiwala, P.D. Kim, S.R. Peyton, A.J. Putnam, ECM compliance regulates osteogenesis by influencing MAPK signaling downstream of RhoA and ROCK, J Bone Miner Res 24(5) (2009) 886-98.

[75] R.M. Salasznyk, R.F. Klees, W.A. Williams, A. Boskey, G.E. Plopper, Focal adhesion kinase signaling pathways regulate the osteogenic differentiation of human mesenchymal stem cells, Exp Cell Res 313(1) (2007) 22-37.

[76] S. Namgung, K.Y. Baik, J. Park, S. Hong, Controlling the growth and differentiation of human mesenchymal stem cells by the arrangement of individual carbon nanotubes, ACS nano 5(9) (2011) 7383-7390.

[77] X. Shi, H. Chang, S. Chen, C. Lai, A. Khademhosseini, H. Wu, Regulating cellular behavior on few-layer reduced graphene oxide films with well-controlled reduction states, Advanced Functional Materials 22(4) (2012) 751-759.

[78] W.C. Lee, C.H.Y. Lim, H. Shi, L.A. Tang, Y. Wang, C.T. Lim, K.P. Loh, Origin of enhanced stem cell growth and differentiation on graphene and graphene oxide, ACS nano 5(9) (2011) 7334-7341.

[79] C. Ge, G. Xiao, D. Jiang, R.T. Franceschi, Critical role of the extracellular signal–regulated kinase–MAPK pathway in osteoblast differentiation and skeletal development, The Journal of cell biology 176(5) (2007) 709-718.

[80] S. Kumar, S.H. Parekh, Molecular Control of Interfacial Fibronectin Structure on Graphene Oxide Steers Cell Fate, ACS Appl Mater Interfaces 13(2) (2021) 2346-2359.

[81] Q. Tu, L. Pang, Y. Chen, Y. Zhang, R. Zhang, B. Lu, J. Wang, Effects of surface charges of graphene oxide on neuronal outgrowth and branching, Analyst 139(1) (2014) 105-15.

[82] A. Halim, L. Liu, A.D. Ariyanti, Y. Ju, Q. Luo, G. Song, Low-dose suspended graphene oxide nanosheets induce antioxidant response and osteogenic differentiation of bone marrow-derived mesenchymal stem cells via JNK-dependent FoxO1 activation, J Mater Chem B 7(39) (2019) 5998-6009.

[83] Y. Chen, Z. Zheng, R. Zhou, H. Zhang, C. Chen, Z. Xiong, K. Liu, X. Wang, Developing a Strontium-Releasing Graphene Oxide-/Collagen-Based Organic-Inorganic Nanobiocomposite for Large Bone Defect Regeneration via MAPK Signaling Pathway, ACS Appl Mater Interfaces 11(17) (2019) 15986-15997.

[84] J. Park, B. Kim, J. Han, J. Oh, S. Park, S. Ryu, S. Jung, J.Y. Shin, B.S. Lee, B.H. Hong, D. Choi, B.S. Kim, Graphene oxide flakes as a cellular adhesive: prevention of reactive oxygen species mediated death of implanted cells for cardiac repair, ACS Nano 9(5) (2015) 4987-99.

[85] M. Sekula-Stryjewska, S. Noga, M. Dzwigonska, E. Adamczyk, E. Karnas, J. Jagiello, A. Szkaradek, P. Chytrosz, D. Boruczkowski, Z. Madeja, A. Kotarba, L. Lipinska, E.K. Zuba-Surma, Graphene-based materials enhance cardiomyogenic and angiogenic differentiation capacity of human mesenchymal stem cells in vitro - Focus on cardiac tissue regeneration, Mater Sci Eng C Mater Biol Appl 119 (2021) 111614.

[86] G.J. Delcroix, P.C. Schiller, J.P. Benoit, C.N. Montero-Menei, Adult cell therapy for brain neuronal damages and the role of tissue engineering, Biomaterials 31(8) (2010) 2105-20.

[87] T.H. Kim, T. Lee, W.A. El-Said, J.W. Choi, Graphene-Based Materials for Stem Cell Applications, Materials (Basel) 8(12) (2015) 8674-8690.

[88] T.H. Kim, S. Shah, L. Yang, P.T. Yin, M.K. Hossain, B. Conley, J.W. Choi, K.B. Lee, Controlling differentiation of adipose-derived stem cells using combinatorial graphene hybrid-pattern arrays, ACS Nano 9(4) (2015) 3780-90.

[89] M. Mariani, S. Shahabi, S. Sieber, G. Scambia, C. Ferlini, Class III beta-Tubulin (TUBB3): More than a Biomarker in Solid Tumors?, Current Molecular Medicine 11(9) (2011) 726-731.

[90] A.V. Gilyarov, Nestin in central nervous system cells, Neurosci Behav Physiol 38(2) (2008) 165-9.

[91] J.A. Kim, N. Lee, B.H. Kim, W.J. Rhee, S. Yoon, T. Hyeon, T.H. Park, Enhancement of neurite outgrowth in PC12 cells by iron oxide nanoparticles, Biomaterials 32(11) (2011) 2871-7.

[92] J. Ericson, P. Rashbass, A. Schedl, S. Brenner-Morton, A. Kawakami, V. van Heyningen, T.M. Jessell, J. Briscoe, Pax6 controls progenitor cell identity and neuronal fate in response to graded Shh signaling, Cell 90(1) (1997) 169-80.

[93] L. Lange, M. Morgan, A. Schambach, The hemogenic endothelium: a critical source for the generation of PSC-derived hematopoietic stem and progenitor cells, Cell Mol Life Sci 78(9) (2021) 4143-4160.

[94] O. Caspi, A. Lesman, Y. Basevitch, A. Gepstein, G. Arbel, I.H. Habib, L. Gepstein, S. Levenberg, Tissue engineering of vascularized cardiac muscle from human embryonic stem cells, Circ. Res. 100(2) (2007) 263-72.

[95] O. Lindvall, Z. Kokaia, A. Martinez-Serrano, Stem cell therapy for human neurodegenerative disorders - how to make it work, Nature Medicine 10(7) (2004) S42-S50.

[96] S.L. Giandomenico, M. Sutcliffe, M.A. Lancaster, Generation and long-term culture of advanced cerebral organoids for studying later stages of neural development, Nat Protoc 16(2) (2021) 579-602.

[97] A. Sarkar, S. Saha, A. Paul, A. Maji, P. Roy, T.K. Maity, Understanding stem cells and its pivotal role in regenerative medicine, Life Sci. 273 (2021) 119270.

[98] M. Borowiak, R. Maehr, S. Chen, A.E. Chen, W. Tang, J.L. Fox, S.L. Schreiber, D.A. Melton, Small molecules efficiently direct endodermal differentiation of mouse and human embryonic stem cells, Cell Stem Cell 4(4) (2009) 348-58.

[99] T. Touboul, N.R. Hannan, S. Corbineau, A. Martinez, C. Martinet, S. Branchereau, S. Mainot, H. Strick-Marchand, R. Pedersen, J. Di Santo, Generation of functional hepatocytes from human embryonic stem cells under chemically defined conditions that recapitulate liver development, Hepatology 51(5) (2010) 1754-1765.

[100] B. Son, H.D. Kim, M. Kim, J.A. Kim, J. Lee, H. Shin, N.S. Hwang, T.H. Park, Physical Stimuli-Induced Chondrogenic Differentiation of Mesenchymal Stem Cells Using Magnetic Nanoparticles, Advanced healthcare materials 4(9) (2015) 1339-1347.

[101] C.M. Metallo, M.A. Vodyanik, J.J. de Pablo, Slukvin, II, S.P. Palecek, The response of human embryonic stem cell-derived endothelial cells to shear stress, Biotechnol Bioeng 100(4) (2008) 830-7.

[102] A.M. Bratt-Leal, R.L. Carpenedo, T.C. McDevitt, Engineering the embryoid body microenvironment to direct embryonic stem cell differentiation, Biotechnol Prog 25(1) (2009) 43-51.

[103] N.S. Hwang, M.S. Kim, S. Sampattavanich, J.H. Baek, Z. Zhang, J. Elisseeff, Effects of three-dimensional culture and growth factors on the chondrogenic differentiation of murine embryonic stem cells, Stem Cells 24(2) (2006) 284-91.

[104] P.W. Burridge, D. Anderson, H. Priddle, M.D. Barbadillo Munoz, S. Chamberlain, C. Allegrucci, L.E. Young, C. Denning, Improved human embryonic stem cell embryoid body homogeneity and cardiomyocyte differentiation from a novel V-96 plate aggregation system highlights interline variability, Stem Cells 25(4) (2007) 929-38.

[105] K. Osafune, L. Caron, M. Borowiak, R.J. Martinez, C.S. Fitz-Gerald, Y. Sato, C.A. Cowan, K.R. Chien, D.A. Melton, Marked differences in differentiation propensity among human embryonic stem cell lines, Nature Biotechnology 26(3) (2008) 313-315.

[106] A. Mouka, B. Arkoun, P. Moison, L. Drevillon, R. Jarray, S. Brisset, A. Mayeur, J. Bouligand, A. Boland-Auge, J.F. Deleuze, F. Yates, T. Lemonnier, P. Callier, Y. Duffourd, P. Nitschke, E. Ollivier, A. Bourdin, J. De Vos, G. Livera, G. Tachdjian, L. Maouche-Chretien, L. Tosca, iPSCs derived from infertile men carrying complex genetic abnormalities can generate primordial germ-like cells, Scientific Reports 12(1) (2022) 1-14.

[107] S. Yaman, M. Anil-Inevi, E. Ozcivici, H.C. Tekin, Magnetic Force-Based Microfluidic Techniques for Cellular and Tissue Bioengineering, Front Bioeng Biotechnol 6 (2018) 192.

[108] S. Galarza, N.P. Birch, L.E. Jansen, K. Bittner, J.D. Schiffman, A.J. Crosby, S.R. Peyton, A 3D biomaterial system to study breast to brain metastasis, 10th World Biomaterials Congress, Frontiers Lausanne, Switzerland, 2016.

[109] S. Sartori, V. Chiono, C. Tonda-Turo, C. Mattu, C. Gianluca, Biomimetic polyurethanes in nano and regenerative medicine, J Mater Chem B 2(32) (2014) 5128-5144.

[110] L. Jia, M. Zhu, C. Kong, Y. Pang, H. Zhang, Q. Qiu, C. Wei, Y. Tang, Q. Wang, Y. Li, Blood neuro-exosomal synaptic proteins predict Alzheimer's disease at the asymptomatic stage, Alzheimer's & Dementia 17(1) (2021) 49-60.

[111] Y. Zhang, S. Chen, Z. Xiao, X. Liu, C. Wu, K. Wu, A. Liu, D. Wei, J. Sun, L. Zhou, H. Fan, Magnetoelectric Nanoparticles Incorporated Biomimetic Matrix for Wireless Electrical Stimulation and Nerve Regeneration, Adv Healthc Mater 10(16) (2021) e2100695.

[112] S. Shahabi, F. Esfarjani, J. Reisi, S. Momenzadeh, M.S. Jami, S. Zamani, The Effects of 8-Week Resistance and Endurance Trainings on Bone Strength Compared to Irisin Injection Protocol in Mice, Adv Biomed Res 10 (2021) 40.

[113] A. Qu, M. Sun, J.Y. Kim, L. Xu, C. Hao, W. Ma, X. Wu, X. Liu, H. Kuang, N.A. Kotov, C. Xu, Stimulation of neural stem cell differentiation by circularly polarized light transduced by chiral nanoassemblies, Nat Biomed Eng 5(1) (2021) 103-113.

[114] G. Paratcha, F. Ledda, C.F. Ibanez, The neural cell adhesion molecule NCAM is an alternative signaling receptor for GDNF family Ligands, Cell 113(7) (2003) 867-879.

국 문 초 록

크기가 조절된 산화 그래핀 플레이크를 이용한 인간줄기세포의 세포 활성 및 분화 조절

박 소 라

서울대학교 대학원

화학생물공학부

세포 인식 장력으로 번역될 수 있는 세포 물리적 자극을 통한 줄기 세포 분화 연구에 대한 관심이 증가하고 있다. 물리적 자극은 기계적 형질도입(mechanotransduction)이라고 하는 인간 중간엽줄기세포 분화를 조절할 수 있는 것으로 알려져 있다. 최근 그래핀의 주요 유도체인 산화 그래핀이 줄기세포 계통 사양에 적합한 물리화학적 특성을 갖는 유망한 물질로 주목되고 있다. 산화 그래핀은 정전기적 소수성 상호작용을 통해 막횡단 수용체 단백질인 인테그린과 상호작용할 수 있다. 그러나 기존 줄기세포 연구에서 사용된 물질은 형태와 크기가 불규칙한 산화 그래핀을 사용하고 있다. 이러한 산화 그래핀 물성의 불규칙성은 산화 그래핀의 측면 크기에 따라 통제되기 어려운 다양한 세포 반응을 일으킨다. 이 연구에서는 볼 밀링 시간을 조정하여 좁은 크기 분포를 가진 흑연을 기계적으로 제작하였다. 그런 다음 수정된 Hummers 의 방법을 사용하여 볼 밀링된 흑연에서 크기가 제어된 산화 그래핀 플레이크를 화학적으로 합성하였다. 합성된 산화

그래핀의 크기 분포는 수용액 환경에서 측정되었다. 인간 줄기 세포에서 크기 조절된 산화 그래핀 플레이크의 용량 의존적 세포독성이 관찰되었다. 산화 그래핀 플레이크와 세포 사이의 상호 작용은 전자현미경 분석되었고 인간 중간엽줄기세포의 골형성 및 신경 분화와 함께 산화 그래핀의 효과를 분석하기 위해 염색 및 유전자 발현을 측정하였다. 또한 면역염색을 통해 세포의 모양과 크기를 분석함으로써 국소적 접착이 줄기세포 분화 촉진과 세포자멸사 촉진 환경에서 세포 생존력 향상에 관여하는 핵심 요소이며 이는 세포 종류와 배양 환경에 따라 다른 크기의 산화 그래핀이 효율적임을 확인하였다. 이로서 크기 조절 산화 그래핀 플레이크가 인간 줄기 세포의 분화 계통 결정 및 치료적 응용을 위한 효율적인 후보가 될 것이라고 제안한다.

주요어: 줄기세포 분화 계통 결정, 산화 그래핀, 골형성 분화, 신경 분화, 세포자멸사, 기계적 형질도입

학번: 2016-21027